

# UC Davis

## UC Davis Previously Published Works

### Title

Time-Fractional Flow Equations (t-FFEs) to Upscale Transient Groundwater Flow Characterized by Temporally Non-Darcian Flow Due to Medium Heterogeneity

### Permalink

<https://escholarship.org/uc/item/0pv0z4t0>

### Journal

Water Resources Research, 57(11)

### ISSN

0043-1397

### Authors

Xia, Yuan  
Zhang, Yong  
Green, Christopher T  
et al.

### Publication Date

2021-11-01

### DOI

10.1029/2020wr029554

Peer reviewed

# Water Resources Research®

## RESEARCH ARTICLE

10.1029/2020WR029554

### Key Points:

- Transient groundwater flow can be temporally non-Darcian and non-stationary in porous media with stationary heterogeneity
- Interconnected high- $K$  channels and isolated low- $K$  deposits caused temporally non-Darcian flow in aquifers
- The distributed time fractional flow equation can upscale the full-range transient groundwater flow

### Correspondence to:

Y. Zhang,  
yzhang264@ua.edu



### Citation:

Xia, Y., Zhang, Y., Green, C. T., & Fogg, G. E. (2021). Time-fractional flow equations (t-FFEs) to upscale transient groundwater flow characterized by temporally non-Darcian flow due to medium heterogeneity. *Water Resources Research*, 57, e2020WR029554. <https://doi.org/10.1029/2020WR029554>

Received 31 DEC 2020

Accepted 5 SEP 2021

## Time-Fractional Flow Equations (t-FFEs) to Upscale Transient Groundwater Flow Characterized by Temporally Non-Darcian Flow Due to Medium Heterogeneity

Yuan Xia<sup>1</sup> , Yong Zhang<sup>2</sup> , Christopher T. Green<sup>3</sup> , and Graham E. Fogg<sup>4</sup> 

<sup>1</sup>College of Environmental Science and Engineering, Guilin University of Technology, Guilin, China, <sup>2</sup>Department of Geological Sciences, University of Alabama, Tuscaloosa, AL, USA, <sup>3</sup>Integrated Modeling and Prediction Division, U.S. Geological Survey, Moffett Field, CA, USA, <sup>4</sup>Hydrologic Sciences, Department of Land, Air and Water Resources, University of California, Davis, CA, USA

**Abstract** Upscaling groundwater flow is a fundamental challenge in hydrogeology. This study proposed time-fractional flow equations (t-FFEs) for upscaling long-term, transient groundwater flow and propagation of pressure heads in heterogeneous media. Monte Carlo simulations showed that, with increasing variance and correlation of the hydraulic conductivity ( $K$ ), flow dynamics gradually deviated from Darcian flow and exhibit sub-diffusive, time-dependent evolution which can be separated into three major stages. At the early stage, the interconnected high- $K$  zones dominated flow, while at intermediate times, the transverse flow due to mixed high- and low- $K$  zones caused delayed rise of the piezometric head. At late times when flow in the relatively high- $K$  domains reached stability, cells with very low- $K$  continued to block the entry of water and generate “islands” with low piezometric head, significantly extending the temporal evolution of the piezometric head. The elongated water breakthrough curve cannot be quantified by the flow equation with an effective  $K$ , the space-fractional flow equation, or the multi-rate mass transfer (MRMT) flow model with a few rates, motivating the development of t-FFEs assuming temporally non-Darcian flow. Model applications showed that both the early and intermediate stages of flow dynamics can be captured by a single-index t-FFE (whose index is the exponent of the power-law probability density function of the random operational time for water parcels), but the overall evolution of flow dynamics, especially the enhanced retention of flow at later times, required a distributed-order t-FFE with variable indexes for different flow phases that can dominate flow dynamics at different stages. Therefore, transient groundwater flow in aquifers with spatially stationary heterogeneity can be temporally non-Darcian and non-stationary, due to the time-sensitive, combined effects of interconnected high- $K$  channels and isolated low- $K$  deposits on flow dynamics (which is the hydrogeological mechanism for the temporally non-Darcian flow and sub-diffusive pressure propagation), whose long-term behavior can be quantified by multi-index stochastic models.

### 1. Introduction

Groundwater flow upscaling is a longstanding topic in hydrogeology, where either the whole model domain or each model grid is homogenized to capture the impact of sub-domain or sub-grid heterogeneity on flow (Durlafsky, 2003; Koltermann & Gorelick, 1996; Rubin & Gómez-Hernández, 1990; Scheibe & Yabusaki, 1998; Wen & Gómez-Hernández, 1996; among many others). This routine modeling task is usually done by upscaling the model parameters: hydrogeologists usually apply Darcy's law-based flow equations (where the groundwater velocity was assumed to be proportional to the hydraulic gradient (Bear, 1978; Whitaker, 1986)) including the Boussinesq equation (for unconfined aquifers with Dupuit assumptions) and the confined groundwater flow equation with effective, equivalent, or interpreted parameters such as the representative hydraulic conductivities to model domain-scale or grid-scale groundwater flow; see the extensive review by Sanchez-Vila et al. (2006).

Recent studies showed that pumping or injection can cause groundwater to flow differently from that described by the Darcy's law-based flow models, motivating the upscaling of groundwater flow using parsimonious flow models as a logical extension to the classical, stochastic flow models (Dagan, 1989; Gelhar, 1993).

Examples of the flow-upscaling method include the continuous-time random walk theory-based diffusion model (Cortis & Knudby, 2006), the multi-rate mass transfer (MRMT) flow model (Municchi & Icardi, 2020; Silva et al., 2009), and the space-fractional flow equation (s-FFE) assuming non-Darcian flow (shown below) (Clout & Botha, 2006; Obember, 2020). A detailed debate of stochastic hydrological approaches including the models mentioned above (especially for pollutant transport) can be seen in Cirpka and Valocchi (2016), Fiori et al. (2016), Fogg and Zhang (2016), Rajaram (2016), and Sanchez-Vila and Fernández-García (2016). Further efforts are still needed to explore the mechanisms and dynamics of long-term transient flow, and then test and improve the parsimonious upscaling models, motivating this study.

We extend the fractional engine (Metzler and Klafter, 2000, 2004), a promising tool originally proposed for solute transport (Zhang et al., 2009), to efficiently upscale long-term groundwater flow. The s-FFE is one of the main fractional-derivative models, and it has been proposed by various researchers to replace Darcy's law-based flow equations to quantify non-Darcy flow (meaning that the groundwater velocity is a non-linear function of the hydraulic gradient) (Clout & Botha, 2006; Mehdinejadi et al., 2013; Obember, 2020; among others). He (1998) was the first to describe non-Darcy flow using a space fractional derivative (see Equation 41 in He (1998)):

$$q_x = -K_x \frac{\partial^\gamma P}{\partial x^\gamma}, \quad (1)$$

where  $q_x$  [ $LT^{-1}$ ] denotes the water flux,  $P$  [ $L^2$ ] is pressure,  $K_x$  [ $T^{-1}$ ] is the fractional hydraulic conductivity, and  $\gamma$  [dimensionless] ( $0 < \gamma \leq 1$ ) is the order of the Riemann-Liouville fractional derivative. The space fractional derivative in Equation 1 is a spatially nonlocal operator and can be expanded to a nonlinear (i.e., power-law) relationship between velocity and the (integer-order) hydraulic gradient; see for example, Zhou and Yang (2018). When  $\gamma = 1$ , Equation 1 reduces to the standard Darcy's law. Non-Darcian flow expressed by Equation 1 and its variants (such as the fractional Swartzendruber model) fit the nonlinear relationship between flux and hydraulic gradient (Qiu et al., 2019; Zhou & Yang, 2018; Zhou et al., 2019) and generalize existing formulas such as the well-known Ergun model (Ergun, 1952), Forchheimer model, and Izbash's equation (Watanabe, 1982) where the hydraulic gradient was assumed to be a power-law function of the bulk flow velocity. Inserting Equation 1 into the continuity equation of seepage flow, one obtains the s-FFE (only the one-dimensional (1D) case is shown here for simplicity):

$$S_s \frac{\partial P}{\partial t} = \frac{\partial}{\partial x} \left( K_x \frac{\partial^\gamma P}{\partial x^\gamma} \right), \quad (2)$$

where  $S_s$  [ $L^{-1}$ ] denotes the specific storage for confined aquifers. The non-Darcian flow Equation 1 is attractive since it leads to the linear flow Equation 2, while the other non-Darcy models may result in nonlinear flow equations. The hydrogeological assumption underlying (2) is that the groundwater flow at a given point of the aquifer is affected by not only local properties of the piezometric field, but also the global spatial distribution of that field (Clout & Botha, 2006).

The s-FFE (2), however, has not been systematically checked against transient flow in aquifers. Most importantly, the space fractional derivative used in the non-Darcian flow Equation 1 assumes unbounded, super-diffusive, fast displacement of water parcels with a power-law leading edge, which may be valid for turbulent flow, for example after flooding events in streams or near a pumping well. Groundwater flow, however, is usually slow with bounded velocities. As will be shown by this study, transient groundwater flow matches the predictions of a time-fractional flow equation (t-FFE) rather than those of s-FFEs including (2), likely due to the delayed pressure propagation and lack of power-law distributed, unbounded velocities in preferential flow paths.

This study fills three knowledge gaps in groundwater flow upscaling with FFEs by (a) exploring how groundwater flow dynamics change with time in heterogeneous porous media under constant forcing terms, (b) upscaling transient water flow based on the long-term evolution of hydraulic head using novel FFEs, and (c) revealing the detailed medium heterogeneity dominating transient groundwater dynamics.

Transient groundwater flow is common in nature. After linking transient flow stages to medium heterogeneity, we will reproduce transient flow dynamics using upscaling models. For comparison purposes, both the deterministic groundwater flow model with upscaling parameters and promising stochastic models will be tested. Researchers in petroleum science (Raghavan, 2011), civil engineering (Deseri & Zingales, 2015), and mathematics (Li et al., 2016) proposed the standard t-FFE with fundamental mathematical analyses,

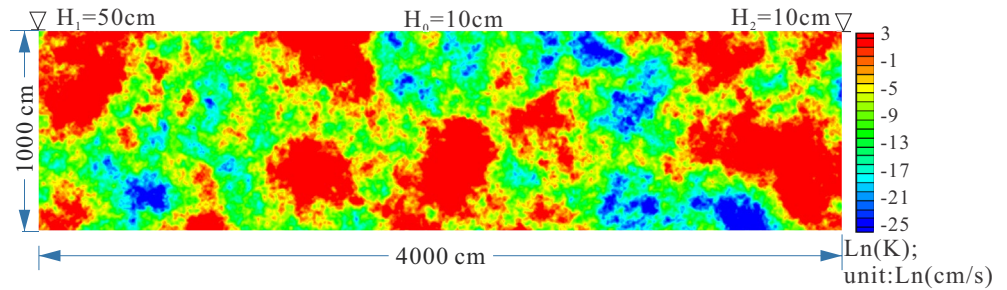


**Figure 1.** Hydraulic conductivity distribution for realization 1 in scenario 9, and the initial head distribution. Notably, here the  $K$ 's range is up to  $\text{Ln}(K)$  of 3 ( $\sim 20$  cm/s), representing the saturated hydraulic conductivity of well sorted gravel (usually in the range of  $10^1$ – $10^2$  cm/s).

but critical questions related to the t-FFE remain unknown, including detailed model derivation, robust solutions under general hydraulic conditions, real-world applicability, parameter upscaling and sensitivity analysis, and hydrogeological mechanisms for transient flow dynamics. This study provides a detailed assessment for the standard t-FFE (from derivation to application), and then improves it for upscaling transient flow, as well as detailed comparison with other models including the standard flow equation, the s-FFE (2), and the general MRMT model.

To reach the goal mentioned above, the rest of this work is organized as follows. Section 2 introduces the Monte Carlo approach used to obtain detailed flow dynamics in porous media with various degrees of heterogeneity. Section 3 checks the feasibility of the standard flow equation and the t-FFE with effective parameters by reproducing the flow dynamics obtained from the Monte Carlo simulations. For comparison purposes, a stochastic flow equation is derived using fractional calculus and is then applied to capture the Monte Carlo results. Section 4 derives a multi-index t-FFE to quantify the complete evolution of transient flow dynamics to improve the single-index t-FFE. Section 5 discusses the mechanisms responsible for the early, intermediate, and late time behaviors of transient flow, which deviate from those predicted by the standard flow equations assuming Darcy's law or the s-FFE model (2). The relationship between non-Darcian flow and non-Fickian pressure propagation, model predictability, velocity distributions, and the relation between flow and transport are also discussed. Conclusions are drawn in Section 6. Model derivation, mathematical analysis, model comparisons, and model limitations are shown in Appendixes A, B, C, and D, respectively.

## 2. Monte Carlo Simulation of Groundwater Flow

### 2.1. Methodology

The Monte Carlo approach used here included two primary steps to estimate water flow in saturated porous media. First, the medium heterogeneity was modeled by standard geostatistical methods. Second, groundwater flow was simulated using MODFLOW-2005 (Harbaugh, 2005), the U. S. Geological Survey's block-centered finite different solver for flow models. All steps were conducted using the software suite, Groundwater Modeling System.

In Step 1, 2D fields for hydraulic conductivity ( $K$ ) were generated (with one example shown in Figure 1), where the random  $K$  was assumed to be log-normal, whose distribution follows an isotropic spherical semi-variogram model (one of the most used models) with zero nugget. The value of  $K$  at the peak of the probability density function (PDF) is equal to  $3.0 \times 10^{-3}$  cm/s, representing gravel/sand (the typical  $K$  ranges for sand and gravel are  $10^{-7}$ – $10^{-2}$  cm/s (Domenico & Schwartz, 1990)). This 2D plane represents a horizontal plane with direction-independent depositional properties. To explore the impact of internal structure of the  $K$  field on flow dynamics, we consider (a) three levels of variance  $\sigma_{\text{Ln}(K)}$  (0.1, 1, and 10), and (b) three levels of correlation range,  $R$ , of the spherical model ( $R$  equal to 10, 100, and 500 cm). The correlation range (or scale) of  $K$  is considered to examine the effects of the scale of the observed domain relative to the scale of geological features. Most importantly, fast flow along the interconnected high- $K$  zones may bring water from distant areas, so that the local variation of flow may be affected by flow at a large range of (upstream)

**Table 1**  
Parameters of the Spherical Semi-Variogram Model for the Nine Scenarios of Heterogeneous  $K$  Fields

Range	Category	$C = 0.1$	$C = 1$	$C = 10$
R = 10 cm	Scenario	Scenario 1	Scenario 2	Scenario 3
	CFE (4)	$K_e = 2.77$	$K_e = 1.95$	$K_e = 0.60$
	FFE (12)	$K_e^* = K_e, \alpha = 1$	$K_e^* = K_e, \alpha = 1$	$K_e^* = 1.9, \alpha = 0.87$
R = 100 cm	Scenario	Scenario 4	Scenario 5	Scenario 6
	CFE (4)	$K_e = 2.93$	$K_e = 2.60$	$K_e = 2.91$
	FFE (12)	$K_e^* = K_e, \alpha = 1$	$K_e^* = K_e, \alpha = 1$	$K_e^* = 31, \alpha = 0.63$
R = 500 cm	Scenario	Scenario 7	Scenario 8	Scenario 9
	CFE (4)	$K_e = 2.98$	$K_e = 2.46$	$K_e = 1.60$
	FFE (12)	$K_e^* = 3.5, \alpha = 0.98$	$K_e^* = 10, \alpha = 0.86$	$K_e^* = 168, \alpha = 0.50$

Note. Also shown are parameters to fit the Monte Carlo simulations by the conventional flow equation (CFE) (4) and the fractional flow equation (FFE) (12). In the legend, “R” (cm) denotes the effective range of  $\text{Ln}(K)$ , “C” ( $\text{Ln}(\text{m/s})$ ) denotes the variance of  $\text{Ln}(K)$ , “ $K_e$ ” ( $\times 10^{-3}$  cm/s) denotes the effective conductivity for the CFE model (4), and “ $K_e^*$ ” ( $\times 10^{-3}$  cm/s $^\alpha$ ) denotes the fractional-order effective conductivity for the FFE model (12).

locations. This is the concept of “spatial nonlocality” (Cushman, 1997), the core assumption underlying the space fractional derivative models (1) and (2).

Hence, a total of nine scenarios with stationarity and various degrees of heterogeneity were generated (see Table 1 and Figure 2). For each scenario, a series of 500 equally probable but different realizations were developed, leading to 4,500  $K$  fields. All realizations have a size of 4,000 cm and 1,000 cm along the longitudinal and transverse directions, respectively, and hence the longitudinal size is 8–400 times larger than the correlation range. The cell size of 10 cm by 10 cm in the longitudinal ( $x$ ) and transverse ( $y$ ) directions was selected to achieve a balance between computational burden and detailed representation of heterogeneity. The 2D model was selected for computational efficiency and for simplicity of visualizing results. Extension of model dimensionality will be discussed in Appendix D.

In Step 2, transient groundwater flow was simulated using the same domain and cell dimensions from the geostatistical realizations. A Dirichlet boundary condition was used for the left and right boundaries to simulate longitudinal flow from the left boundary (with a constant head of 50 cm) to the right boundary (with a constant head of 10 cm) with the initial head of 10 cm, resulting in a general hydraulic head gradient parallel to the longitudinal direction (Figure 1). The remaining domain boundaries are impermeable boundaries. The mathematical model for the transient flow process is the classical groundwater flow equation with initial and boundary conditions defined below:

$$S_s \frac{\partial H(x, y, t)}{\partial t} = \frac{\partial}{\partial x} \left[ K_{xx}(x, y) \frac{\partial H(x, y, t)}{\partial x} \right] + \frac{\partial}{\partial y} \left[ K_{yy}(x, y) \frac{\partial H(x, y, t)}{\partial y} \right] \quad (3a)$$

$$H(x, y, t = 0) = H_0(x, y) \quad (3b)$$

$$H(x, y, t) |_{x=x_l} = H_l \quad (3c)$$

$$H(x, y, t) |_{x=x_r} = H_r \quad (3d)$$

$$\frac{\partial}{\partial y} H(x, y, t) |_{y=y_b} = 0; \quad \frac{\partial}{\partial y} H(x, y, t) |_{y=y_t} = 0 \quad (3e)$$

where the specific storage coefficient  $S_s$  is constant and equal to 0.001 in this study;  $K_{xx}$  and  $K_{yy}$  [ $LT^{-1}$ ] denote the conductivity components along the  $x$  and  $y$  directions, respectively;  $H(x, y, t = 0)$  (=10 cm) denotes the initial distribution of the hydraulic head;  $x_l$  and  $x_r$  denote the left and right boundaries of the domain, respectively;  $y_b$  and  $y_t$  denote the minimum and maximum coordinates along the  $y$ -axis, respectively; and  $H_l$  (=50 cm) and  $H_r$  (=10 cm) denote the constant head at the left and right boundaries, respectively.



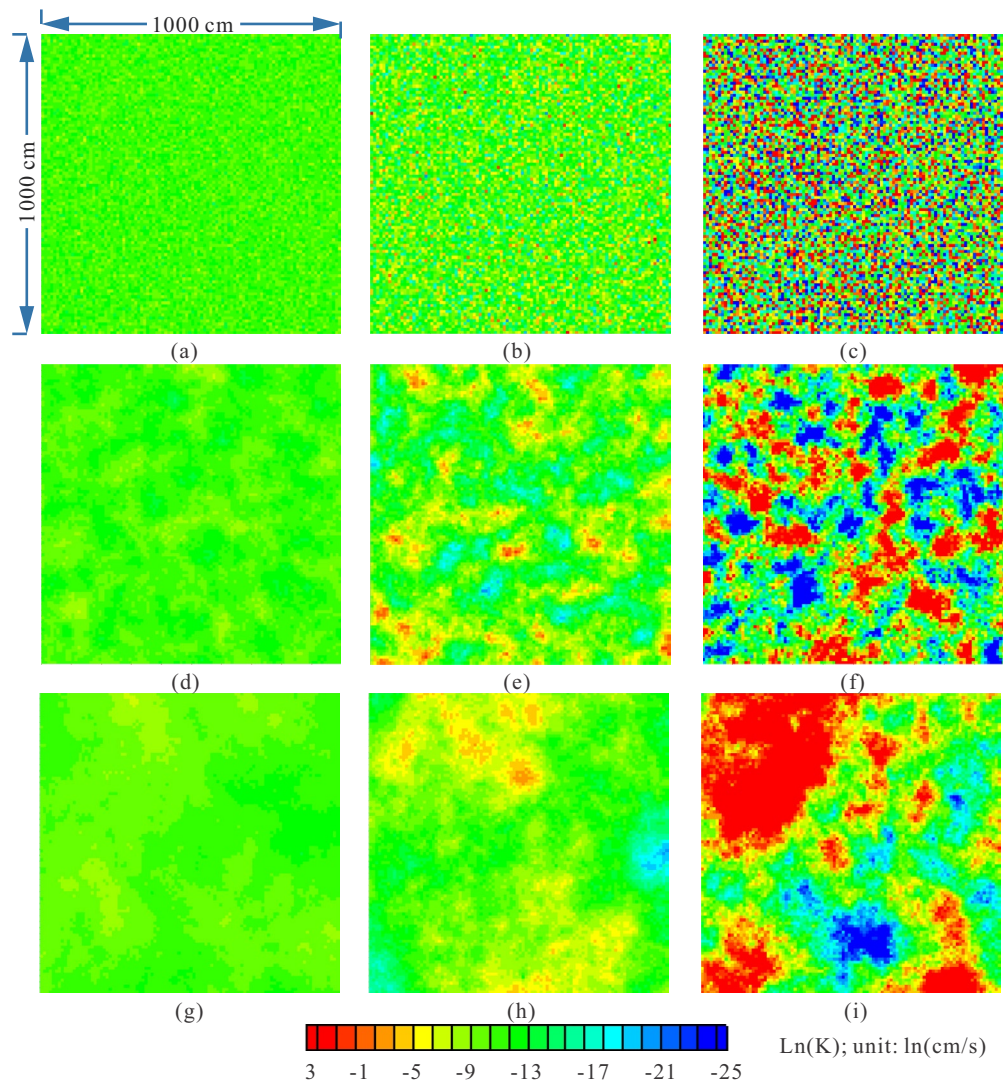


**Figure 2.** The simulated  $\text{Ln}(K)$  distribution for realization #1 for all nine scenarios. Plots (a~i) represent scenarios 1~9, respectively. Note that for a clear view, only the first 1,000 cm is shown for the full 4,000 cm extend along the longitudinal direction.

The relatively large general hydraulic head gradient (0.01) was used to obtain complete flow dynamics within the modeling period of  $1 \times 10^6$  seconds. The impact of the general hydraulic head gradient on flow dynamics will be discussed in Section 3.3. Ensemble averages of transient hydraulic head at various downstream control planes were calculated and analyzed below.

## 2.2. Monte Carlo Simulation Results

Numerical results of the Monte Carlo simulations show that groundwater dynamics transition from piston-like flow to meandering, channel-like flow with the increase of the variance of  $\text{Ln}(K)$  and the effective range  $R$  (Figure 3). For example, for scenario 1 with the smallest variance and the shortest effective range, water moves almost parallel to the longitudinal axis with a uniform velocity (Figure 3a), which is explained in Sections 3.3 and 5.5. With the increase of  $\text{Ln}(K)$  variance in scenarios 2 and 3 (while the effective range remains unchanged), the greater  $K$ -contrast forces more water into the high- $K$  zones, generating more channelled flows (Figures 3b and 3c). Multiple channels with similar capacity to conduct water are generated, resulting in a relatively uniform network filled with thin and short channels due to the small effective range  $R$  (Figures 3b and 3c). Because there are many thin flow channels, the average direction of flow at any

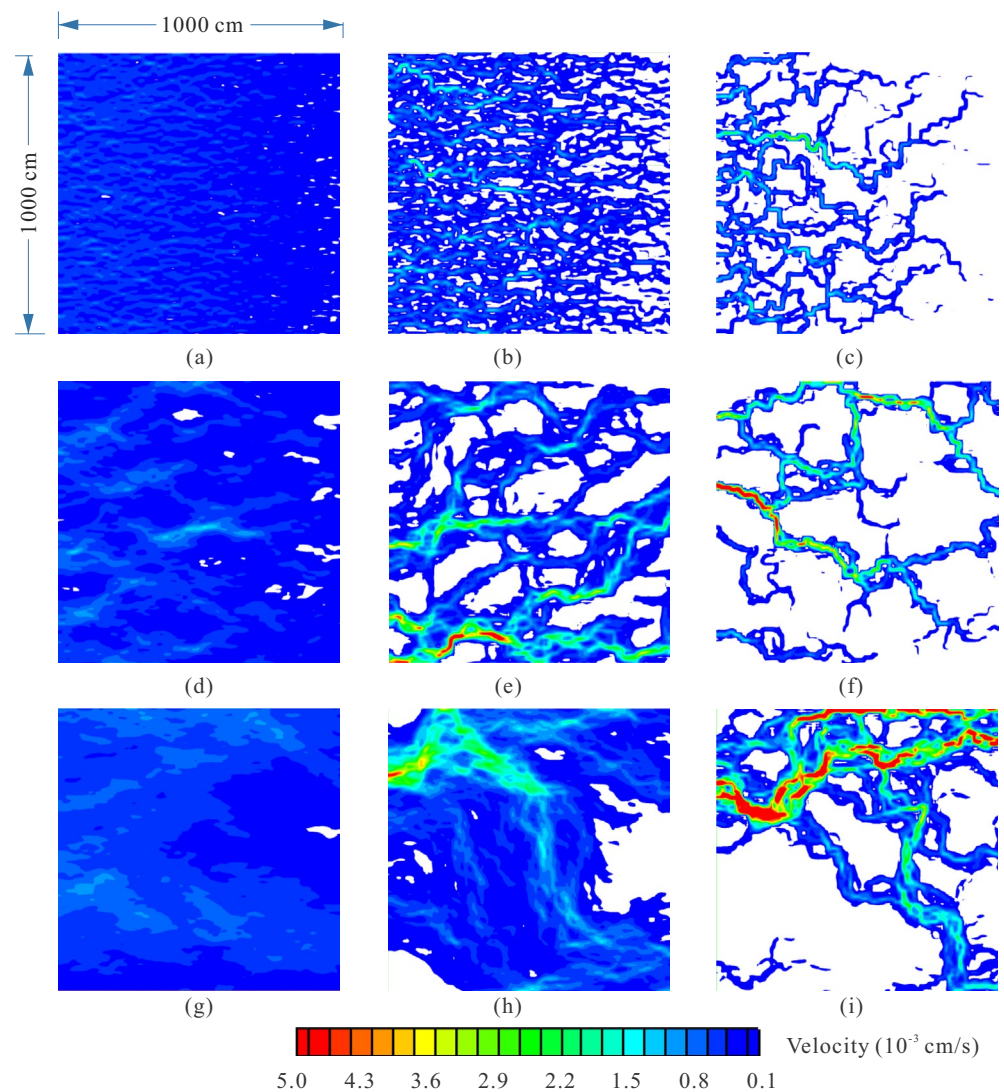


**Figure 3.** The simulated flow velocity for realization #1 for all the nine scenarios at time  $t = 1,000$  s. The white regime represents low velocity zones (i.e., relatively immobile zones) with velocity lower than  $0.1 \times 10^{-3}$  cm/s. Plots (a~i) represent scenarios 1~9, respectively. For illustration purposes, only the first 1,000 cm is shown for the full 4,000 cm extend along the longitudinal direction in these plots.

longitudinal distance is approximately parallel to the no-flow boundaries. When both the variance of  $\text{Ln}(K)$  and the effective range  $R$  increase, a smaller number of dominant channels occurs and the transverse velocity can increase significantly, resulting in complex patterns filled with elongated, sinuous flow paths. Water from the left boundary (the upgradient boundary) tends to converge into discrete flow pathways while moving downgradient, different from the dispersed, parallel flow observed in scenarios 1~3 (Figures 3f and 3i).

Hydraulic head evolution at various control planes (located at  $x = 1,000, 2,000,$  and  $3,000$  cm) also revealed enhanced tailing behavior in piezometric head with an increasing variance of  $\text{Ln}(K)$  and effective range  $R$  (Figure 4). For example, for scenario 1 representing the most “homogeneous” media, the transient head curve, which is called the “water Breakthrough Curve” (BTC) in this study and represents the temporal evolution of piezometric head (which is the mean of the heads in all cells along the control plane), is relatively steep (Figure 4a), due to the piston-like flow pattern. The water BTC (which may also represent energy breakthrough when the hydraulic head represents potential energy) can be defined mathematically as  $\bar{H}(x, t) = \frac{1}{y_t - y_b} \int_{y_b}^{y_t} H(x, y, t) dy$ , where  $y_t$  and  $y_b$  (used also to define the boundaries for the classical flow model

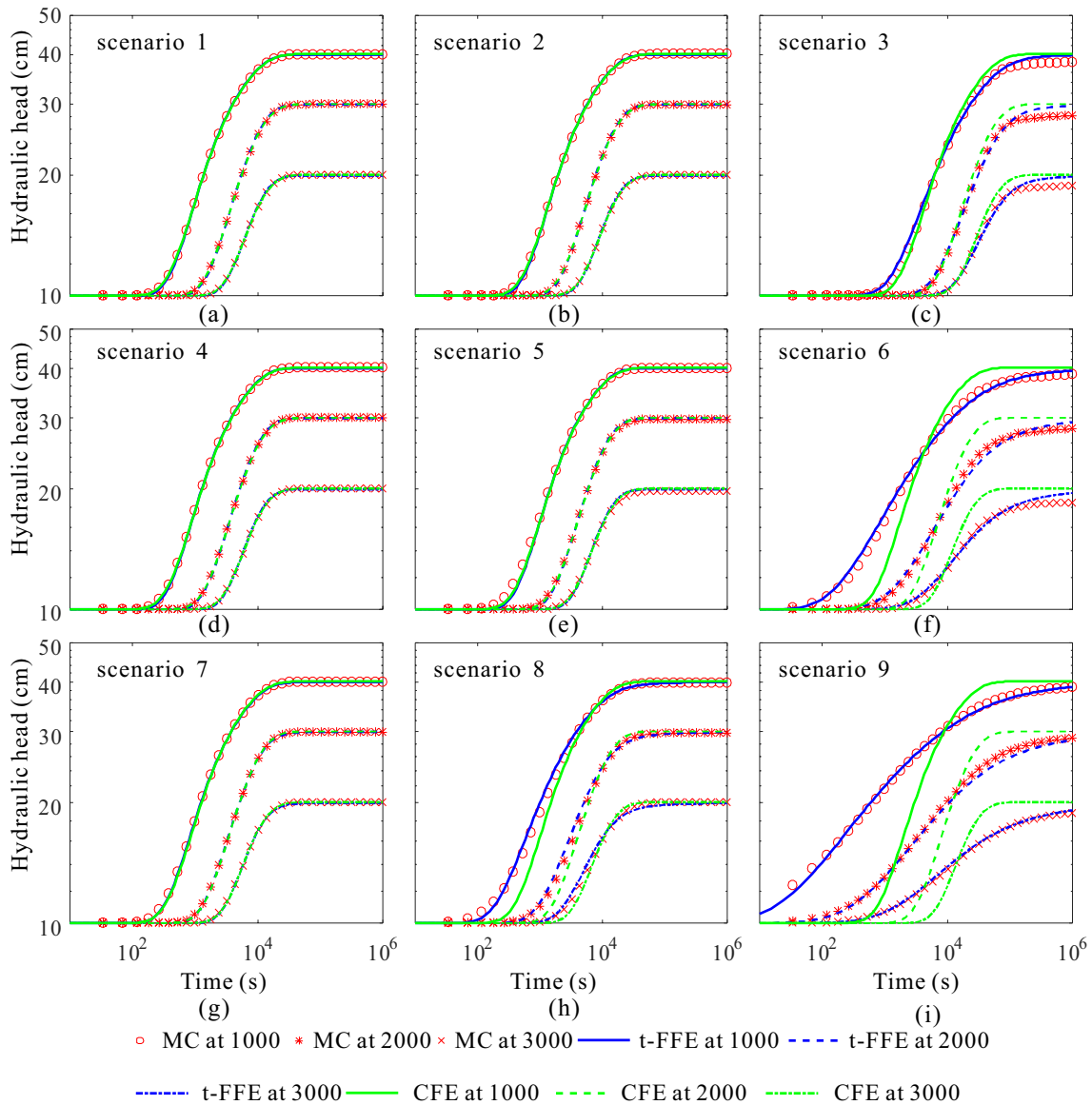


**Figure 4.** The transient piezometric head at three control planes (i.e., mean of the heads in all cells along the control plane) (located at  $x = 1,000, 2,000,$  and  $3,000$  cm) for all nine scenarios in a log-log plot: Monte Carlo simulations (symbols) versus model results (lines) using both the Conventional Flow Equation (CFE) model (4) and the Time Fractional Flow Equation (t-FFE) model (12).

(3)) are the  $y$ -coordinates at the top and bottom of the control plane, respectively. Hydraulic head can rise relatively quickly and then stabilize, implying relatively smooth propagation of hydrostatic pressure through the medium. For scenario 9 with strong variation of  $\text{Ln}(K)$  and high correlation (i.e., larger  $R$ ), analysis of water movement (see for example Figure 3i) reveals that the velocity of the waterfront increased due to dominant preferential pathways with lower tortuosity, while water retained in relatively low-permeability zones was also delayed (discussed further in Section 5.2). Hence, both the early arrivals and delayed flow can be observed for scenario 9, producing an elongated water BTC (Figure 4i). Notably, the hydraulic head did not stabilize in scenario 9 even at the end of the modeling period ( $10^6$  s). Here the “tailing behavior” means that the water BTC tail (at the early and/or late time) is heavier than that estimated by the Darcy’s law based classical flow model, which is analogous to the well documented tailing behavior in the pollutant transport BTC (Zhang et al., 2009).

It is also noteworthy that the Monte Carlo results provide information about a potential threshold for (or the upper limit on) the variance of  $\text{Ln}(K)$ , denoted as  $\sigma_{\text{Ln}(K)}^*$ , for generating non-Darcian flow dynamics (the



“non-Darcian flow dynamics” are characterized by the elongated late-time BTC tail shown in Figure 4i). For porous media with the  $\text{Ln}(K)$  variance below  $\sigma_{\text{Ln}(K)}^*$ , the transient head will not exhibit any apparent tailing behavior, regardless of the magnitude of the correlation range, since the variation of  $\text{Ln}(K)$  is not strong enough to form any apparent preferential flow pathways. Only when the  $\text{Ln}(K)$  variance is above  $\sigma_{\text{Ln}(K)}^*$  will apparent channeled flow appear. In this study, this threshold  $\sigma_{\text{Ln}(K)}^*$  is found to be no larger than 0.1 (with units of  $\text{Ln}(\text{cm/s})$ ). This threshold, however, contains high uncertainty, due to the limited scenarios (9 total) built in this study. A quantitative, strict criterion for the definition of  $\sigma_{\text{Ln}(K)}^*$  requires many more scenarios and a systematic modeling analysis, which is beyond the focus of the current work and can be pursued independently. In addition, if the water BTC corresponding to the test  $\text{Ln}(K)$  variance exhibits a visible discrepancy at the tailing portion as compared to the classical flow equation, we refer to it as an “apparent tailing behavior.” The corresponding hydrogeologic interpretation is that the piston-type water flow changed gradually to a more complex flow dominated by channelized flow.

### 3. Upscaling With Deterministic and Stochastic Models

This section develops physical models with spatially independent, effective parameters to upscale flow dynamics. We focus on 1D effective models, which may recover the transient head observed in the Monte Carlo simulations shown above (Figure 4).

#### 3.1. Conventional Flow Equation With Effective $K$ for Upscaling Groundwater Flow

The Conventional Flow Equation (CFE) with the effective  $K$  takes the form:

$$\frac{\partial \bar{H}(x,t)}{\partial t} = \frac{K_e}{S_s} \frac{\partial^2 \bar{H}(x,t)}{\partial x^2}, \quad (4)$$

where  $\bar{H}(x,t)$  denotes the column (transversely)-averaged hydraulic head, and  $K_e [LT^{-1}]$  is the effective hydraulic conductivity.

The upscaling of hydraulic conductivity of heterogeneous media has been a topic in hydrology for over a century (Pinczewski & Paterson, 2002). Various methods have been developed in the last four decades to estimate the equivalent permeability/hydraulic conductivity (which is a constant permeability/hydraulic conductivity tensor that generates the same flow as the heterogeneous medium at the boundaries of the domain) or effective permeability/hydraulic conductivity (an intrinsic physical magnitude that is used for a statistically homogeneous medium and is independent of the macroscopic boundary conditions) for saturated porous media (Renard & de Marsily, 1997). Extensive reviews by Garboczi (1990), Wen and Gómez-Hernández (1996), Renard and de Marsily (1997), and Sanchez-Vila et al. (2006) identified the advantages and disadvantages of the upscaling methods. For example, as commented by Renard and de Marsily (1997), the heuristic, deterministic, and stochastic methods are the three main methods for upscaling steady-state flow. Although these methods can provide a reasonable range of the equivalent or effective hydraulic conductivity, the heuristic method (which calculates the mean hydraulic conductivity using for example the power average or averaging means) tends to neglect geometric structure of medium heterogeneity during the upscaling process (Knudby et al., 2002). The deterministic method (which assumes that the geological model is perfectly known) works better for media with weak heterogeneity (Renard & de Marsily, 1997), and the stochastic method (which assumes medium properties to be random variables) is generally based on assumptions not always valid for natural media (Dagan, 1993; Dykaar & Kitanidis, 1992; Gelhar & Axness, 1983). Recent studies also developed experimental techniques (Cai et al., 2012; Kendrick et al., 2021; Strangfeld, 2020; Wei et al., 2021), hydraulic tomography (Bellin et al., 2020), deep learning (Moghaddam, 2020), as well as multi-scale characterization (Colecchio et al., 2020), among other approaches, to define the effective hydraulic conductivity. Here we select the Monte Carlo simulation of groundwater flow to calculate the effective hydraulic conductivity  $K_e$  for two reasons. First, it can provide the accurate  $K_e$  although the process is computationally demanding. Second and most importantly, we will show that the effective hydraulic conductivity typically used in flow models cannot upscale non-Darcian flow in strongly heterogeneous porous media.

To obtain  $K_e$ , we first calculated the steady-state flux for each 2D heterogeneous  $K$  field (by rerunning MODFLOW), and then obtained the ensemble average of the steady-state flux  $F^*$  (the steady-state flux for each

realization is the vertically integrated total flux across each control plane when the groundwater flow model stabilizes) for each scenario (note that for scenario 9, a longer modeling time,  $10^9$  s, was needed and used to approximate the steady-state condition). We then applied Darcy's law to calculate the effective parameter  $K_e = F^*/J$ , where  $J$  is the general hydraulic gradient (equal to 0.01 for all scenarios). The resultant  $K_e$  listed in Table 1 shows that, on one hand, when the variance of  $\text{Ln}(K)$  is relatively small (i.e.,  $\sigma_{\text{Ln}(K)} = 0.1$ , for scenarios 1, 4, and 7), water moves slightly faster with an increasing correlation range of  $K$  (resulting in a larger effective conductivity  $K_e$ ), due to the slightly enhanced channels in the longitudinal direction. This is expected. On the other hand, when the correlation range of  $K$  is relatively small (i.e.,  $R = 10$  cm, for scenarios 1, 2, and 3), the increase of the variance of  $\text{Ln}(K)$  can generate more low- $K$  blocks, and water must bypass these almost impermeable blocks (which can overshadow the fast flow due to the increased number of high- $K$  blocks when the variance of  $\text{Ln}(K)$  increases), resulting in a lower stable total flux and  $K_e$ . Hence, the variance and correlation range of  $K$  tend to exert different impacts on the effective conductivity  $K_e$ . With an increasing variance and correlation range of  $K$ , the competition between the two factors can cause complex variation of  $K_e$ , as shown in Table 1.

After  $K_e$  is defined, we apply the CFE (4) to predict the temporal evolution of the hydraulic head for each scenario. With the following boundary and initial conditions similar to (3):

$$\bar{H}(x, t = 0) = H_0, \quad (5a)$$

$$H(x, t) \big|_{x=x_l} = H_l \quad (5b)$$

$$H(x, t) \big|_{x=x_r} = H_r \quad (5c)$$

the analytical solution for the CFE (4) is:

$$\bar{H} = H_r + (H_l - H_r) \frac{2}{\pi} \sum_{n=1}^{\infty} \frac{1}{n} \sin\left(\frac{n\pi}{L}x\right) \cdot \left(1 - e^{-\frac{K_e n^2 \pi^2}{S_s L^2}t}\right). \quad (6)$$

### 3.2. Generalized, Time-Nonlocal Darcian Flow to Derive the Upscaled Flow Model

For comparison purposes, we also developed a model of time-nonlocal upscaled flow based on the following observations. Figure 4 shows that the water BTCs are relatively flat for porous media with a larger variance and a longer correlation range of  $K$ , showing that the hydraulic head starts rising more immediately and rises more gradually than that of scenarios with a smaller variance and a shorter correlation range of  $K$ . Hence, the water might have been retained in low- $K$  zones for a period of time, an impact similar to the memory effect reported by Cortis and Knudby (2006) for groundwater flow in confined aquifers. Comparing Figures 3 and 4 shows that increased abundance of transverse channels results in a lower slope of the water BTC (i.e., stronger temporal memory). Further analysis shows that the transverse velocity fluctuates across several orders of magnitude for Scenario 9 (Figure 5), and therefore different water parcels may spend different periods of time while crossing the same column, resulting in a strong memory effect and late time tailing of the water BTC.

In a traditional 1D upscaled model (such as the CFE (4)), differences of head in a column of cells perpendicular to the main flow direction may not be captured by an average head assigned to the representative longitudinal cell. Water can redistribute in a column of cells, while the average head remains unchanged. Only water movement from one column to another can change the average head at that column. This helps to explain the memory effect (meaning the persistent water head, or the BTC tailing behavior). Water can translocate perpendicularly to the main flow direction without contributing to the change of the average head; from the standpoint of average heads and flows, the water parcels appear to be trapped. In other words, the history of water redistribution at the local position can affect the current propagation of pressure or water mass at this position (or water fluxes in and out of the same position), which describes the impact of "time nonlocality" on groundwater flow (Cushman, 1997). Additional treatment is therefore needed in the 1D upscaled model to account for the impact of cross-section heterogeneity on flow dynamics. For example, the differential transverse flow paths and travel periods can be interpreted as water trapped or retained by the column for random amounts of time using a new stochastic model.

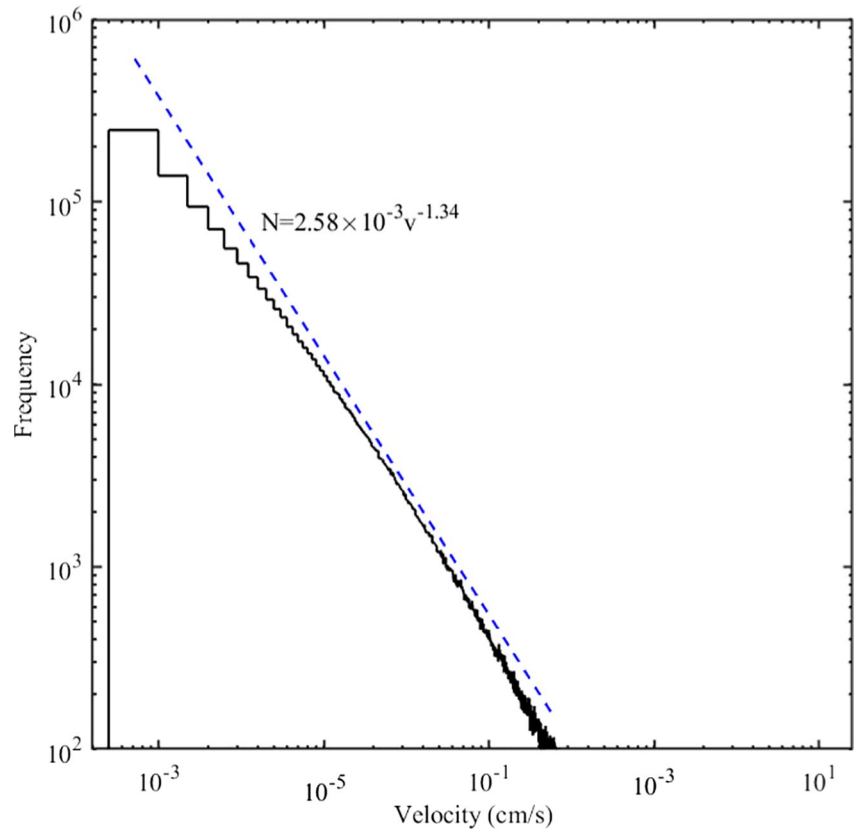


**Figure 5.** Frequency of the transverse velocity in scenario 9. The dashed line shows the best-fit trendline using a power-law function.

Based on the analyses shown above, we propose a stochastic flow model that accounts for memory effects in water movement. The continuity equation of water flow can be written as:

$$S_s \frac{\partial \bar{H}(x, t)}{\partial t} = -\frac{\partial q(x, t)}{\partial x}, \quad (7)$$

where the water flux  $q(x, t)$  is expressed by the following generalized, time-nonlocal Darcy's law (which defines the “temporally non-Darcian flow”; see Section 5.3):

$$q(x, t) = -K_e^* \int_0^t \frac{\partial \bar{H}(x, s)}{\partial x} [\delta(t-s) - G(t-s)] ds, \quad (8)$$

where  $\delta$  is the Dirac delta function, and  $G(t)$  denotes the memory function. Here the water flux  $q(x, t)$  can be divided into two parts. The first part in the integral including the Dirac delta function is the immediate contribution (at time  $t$ ) from the present longitudinal head gradient, expressed by  $-K_e^* \partial \bar{H} / \partial x$  following the classical, time-local, Darcy's law. The second part is due to the delayed response of water flowing through (transverse) columns from time 0 to  $t$  (i.e., the whole history), which can be quantified by the convolution  $K_e^* \int_0^t [\partial \bar{H}(x, s) / \partial x] G(t-s) ds$ , a time nonlocal term.

Substituting Equation 8 into Equation 7 and taking Laplace transform ( $t \rightarrow \tau$ ), one obtains:

$$S_s [\tau \tilde{\bar{H}}(x, \tau) - \bar{H}_0(x)] = K_e^* \frac{\partial^2 \tilde{\bar{H}}(x, \tau)}{\partial x^2} [1 - \tilde{G}(\tau)], \quad (9)$$

where the tilde represents the Laplace transform, and  $\bar{H}_0(x)$  denotes the initial hydraulic head at position  $x$ . Here the memory function  $G(t)$  accounts for the probability of water parcels staying in the transverse column for time  $t$ , which is an upscaled parameter assumed to be independent of position  $x$  for stationary media. The explicit expression of  $G$ , however, is uncertain due to the complex retention processes and

memory effects. Figure 5 reveals that  $G$  may have a power-law declining tail. Moreover, this function accounts for the ensemble average of the retention time distribution of hundreds of realizations, so it may obey the law of large numbers and converge to the half-axis stable distribution, which has an explicit Laplace transform:

$$\tilde{G}(\tau) = e^{-\tau^\gamma}, \quad (10)$$

where the exponent  $\gamma$  is between 0 and 1.

Substituting Equation 10 into Equation 9, we have

$$S_s(\tau\tilde{H} - \bar{H}_0) = K_e^* \frac{\partial^2 \tilde{H}}{\partial x^2} \left[ 1 - e^{-\tau^\gamma} \right]. \quad (11)$$

When  $\tau \rightarrow 0$  (representing  $t \rightarrow \infty$ ), one has  $1 - e^{-\tau^\gamma} \rightarrow \tau^\gamma$ , and hence Equation 11 leads to the following t-FFE (after taking the inverse Laplace transform):

$$\beta^* \frac{\partial^\alpha \bar{H}(x,t)}{\partial t^\alpha} = \frac{K_e^*}{S_s} \frac{\partial^2 \bar{H}(x,t)}{\partial x^2}, \quad (12)$$

where the index  $\alpha = 1 - \gamma$ , and the constant factor  $\beta^* = 1 [T^{\alpha-1}]$  is added here for units conversion. Hence, the effective hydraulic conductivity  $K_e^*$  has the commonly used units for hydraulic conductivity [ $LT^{-1}$ ], which is more easily interpreted than the fractional hydraulic conductivity  $K_x [L^\gamma T^{-1}]$  in Equation 2 whose hydrogeologic interpretation remains unclear. For description simplicity, the units converter  $\beta^*$  is no longer shown in the following formulas ( $\beta^*$  is “absorbed” by the effective hydraulic conductivity  $K_e^*$ ). When  $\alpha = 1$ , the t-FFE (12) reduces to the CFE (4).

To justify the t-FFE (12) built upon the assumed time-nonlocal Darcy’s law (8), we derived the t-FFE (12) using the time subordination approach (Appendix A), which also reveals the form of the temporal non-Darcian flow and will be discussed further in Section 5.3.

With the boundary and initial conditions defined by Equation 5, the t-FFE model (12) has an analytic solution:

$$\bar{H} = H_r + (H_l - H_r) \frac{2}{\pi} \sum_{n=1}^{\infty} \frac{1}{n} \sin\left(\frac{n\pi}{L} x\right) \cdot \left[ 1 - E_\alpha\left(-\frac{K_e^* n^2 \pi^2}{S_s L^2} t^\alpha\right) \right], \quad (13)$$

where  $E_\alpha$  denotes the Mittag-Leffler function.

### 3.3. Model Application and Comparison

Applications show that the CFE model (4) predicts the temporal change of the hydraulic head for scenarios with a relatively small variance of  $\text{Ln}(K)$  and a relatively short correlation range (including scenarios 1, 2, 4, 5, and 7) (Figure 4). For strongly heterogeneous  $K$  fields with a larger variance and correlation range (including scenarios 3, 6, and 9), the CFE (4) not only underestimates the early arrival of water parcels moving along preferential flow pathways, but also underestimates the late-time arrivals of water parcels trapped previously by low- $K$  zones. Note that the CFE (4) cannot significantly change the slope of the water BTC in a log-log plot by increasing the effective hydraulic conductivity  $K_e$ . This is because the slope of the water BTC is not sensitive to the effective hydraulic conductivity, although an increasing  $K_e$  results in an earlier tail in the water BTC (Figure 6). This is expected considering the analytical solution 6. According to (6), the maximum slope of the simulated water BTC in a log-log plot appears at time  $t = \frac{S_s}{K_e} \frac{L^2}{n^2 \pi^2}$  (so that the water BTC shifts toward younger ages (i.e., shorter travel times) with an increasing  $K_e$ ), and the maximum slope of the water BTC can be approximated by  $\propto (H_l - H_r) \frac{2}{\pi} \sin\left(\frac{\pi}{L} x\right) e^{-1}$  (so that the maximum slope does not change with  $K_e$  in a log-log plot, as shown in Figure 6). Therefore, the CFE (4) cannot capture the water BTCs whose slope changes with the medium heterogeneity.

The t-FFE model (12) with the best-fit index  $\alpha$  and effective conductivity (denoted as  $K_e^*$  to be distinguished from the effective conductivity  $K_e$  used in the CFE model (4)) listed in Table 1 can capture the overall trends of the water BTCs (see the blue lines in Figure 4). It is not possible to predict  $K_e^*$ , except for fitting the



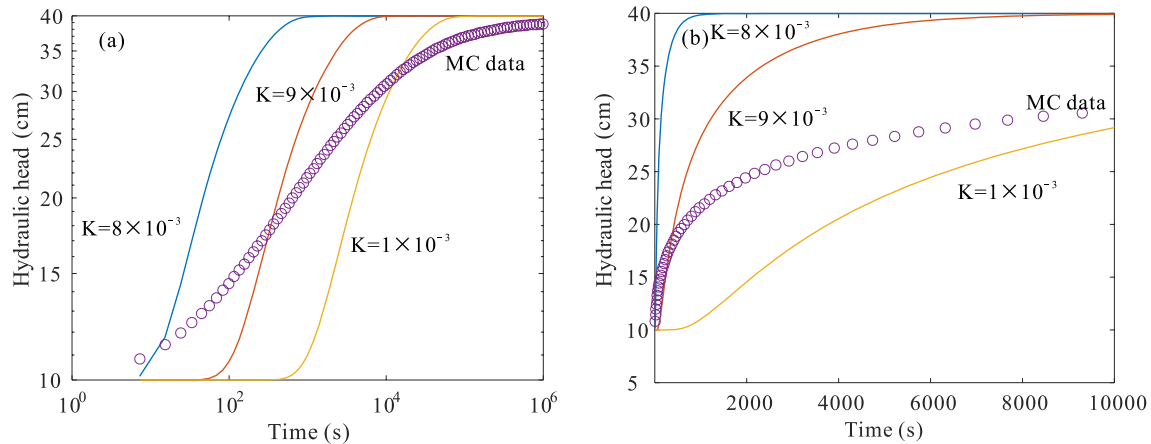


**Figure 6.** Sensitivity scenarios of the simulated water BTC using the Conventional Flow Equation (CFE) model (4) with different  $K_e$  (units: cm/s) for scenario 9. (a) Is a log-log plot, and (b) is a linear-linear plot. The symbols and lines represent the Monte Carlo data and the CFE (4) solutions, respectively.

measured water BTC or when the index  $\alpha = 1$  in the t-FFE (2). When  $\alpha = 1$  (i.e., for the medium with weak heterogeneity),  $K_e^*$  reduces to the classical effective hydraulic conductivity that may be predicted. When  $\alpha < 1$  (i.e., for the medium with weak heterogeneity), both the index  $\alpha$  (which cannot be directly measured; see further discussion in Section 5.4) and  $K_e^*$  affect the shape of the water BTC. The same challenge exists for the effective dispersion coefficient in the fractional-derivative models for pollutant transport, which remains a scale-dependent fitting parameter to compensate for the missing local velocity in a macroscopic model (Zhang et al., 2020). To further check the predictability of the best-fit parameters in the t-FFE (12), we predicted the water BTC using scenario 3 but with the general hydraulic gradient reset to 0.02 and 0.001 in the Monte Carlo simulations. Results show that the t-FFE (12) with the fractional index  $\alpha$  and the fractional conductivity  $K_e^*$  fitted for the general head gradient of 0.01 can successfully predict the flow dynamics for other general head gradients (Figure 7).

The t-FFE (12) with a single index  $\alpha$ , however, overestimates the late-time speed of water motion for some scenarios with large correlation ranges (scenarios 3 and 6) (notably, this overestimation is not apparent in scenario 9, because it takes longer for the retention effect to appear in scenario 9) (Figure 4). Hence, a

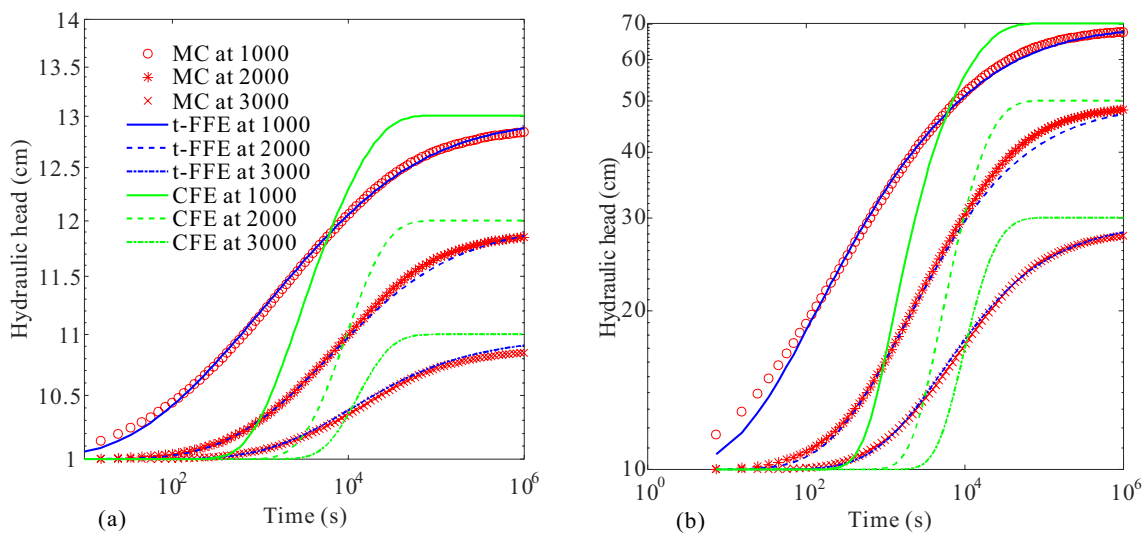


**Figure 7.** The Monte Carlo data (symbols) versus the best-fit water BTC using the Conventional Flow Equation 4 and the t-FFE (12) (lines) for scenario 9 when the hydraulic head gradient is 0.001 (left) or 0.02 (right). The t-FFE (12) with all the two parameters (the fractional index  $\alpha$  and the fractional conductivity  $K_e^*$ ) fitted for the general head gradient of 0.01 is used here to predict the water BTCs generated by the Monte Carlo simulations with a different general head gradient (0.001 and 0.02).

new t-FFE with multiple scaling rates might be needed for transient water flow, especially to capture the enhanced water retention at late times (with hydrogeological explanation discussed in Section 5.2), motivating the distributed-order fractional-derivative model discussed below.

#### 4. Full-Range Transient Flow Using a Distributed-Order Fractional Flow Equation (d-FFE)

To capture the distinct impacts of relatively high- $K$  and low- $K$  materials on transient flow dynamics, we separate the saturated porous media into mobile and relatively immobile zones, with the corresponding hydraulic head denoted as  $H_m(x, t)$  and  $H_{im}(x, t)$ , respectively. Dynamics of the mobile zone, consisting of the major flow paths, may be affected by the slow mass exchange with the surrounding low-permeability zones. Following the concept of the mobile-immobile flow model (Silva et al., 2009), we propose a governing equation for the head in the mobile zone ( $H_m$ ):

$$\frac{\partial^{\alpha_1} H_m(x, t)}{\partial t^{\alpha_1}} = \frac{K_e^*}{S_s} \frac{\partial^2 H_m(x, t)}{\partial x^2} - \frac{1 - \beta}{\beta} \frac{K_{im}}{S_s} [H_m(x, t) - H_{im}(x, t)], \quad (14)$$

where the suffix “ $m$ ” and “ $im$ ” of  $H$  represent the hydraulic head in the mobile and immobile phases, respectively;  $\beta$  [dimensionless] denotes the volumetric proportion of the mobile zone;  $(1 - \beta)/\beta$  represents the ratio of immobile to mobile volume, which is similar to the concept of the capacity coefficient used for the MRMT model for chemical transport (Haggerty et al., 2000); and  $K_{im}$  denotes the effective hydraulic conductivity for the immobile zone.

The relatively immobile zone contains low- $K$  cells with small to even negligible flow rates. Monte Carlo results in Section 2 showed that the water flow rate within the immobile zone is very small, and the temporal change of hydraulic head in the immobile zone is mainly due to the mass exchange between mobile and immobile flow zones. These results motivate us to propose the following fractional-derivative model to describe the evolution of the immobile hydraulic head ( $H_{im}$ ):

$$\frac{\partial^{\alpha_2} H_{im}(x, t)}{\partial t^{\alpha_2}} = \frac{K_{im}}{S_s} [H_m(x, t) - H_{im}(x, t)], \quad (15)$$

where the index  $\alpha_2$  can be different from the index  $\alpha_1$  used in the mobile model (14) to capture different effects of mobile and immobile phases on the overall flow dynamics. Here the index  $\alpha_2$  characterizes the residence time distribution of water trapped in the low-permeability islands (described in Section 5.2). Specifically,  $\alpha_2$  defines the exponent of the power-law PDF for this residence time distribution. The effective hydraulic conductivity  $K_{im}$  characterizes the capacity of mass exchange between the low-permeability islands and the surrounding materials. Although these parameters have clear physical meanings, they cannot be measured directly at present and must be fitted. The same limitation (i.e., poor parameter predictability) persists for most nonlocal, upscaling transport models (Zhang et al., 2020). Empirical approximation of model parameters will be discussed in Section 5.4.

The total hydraulic head,  $H_{tot}$ , is a weighted summation of the mobile and immobile head:

$$H_{tot}(x, t) = \beta H_m(x, t) + (1 - \beta) H_{im}(x, t). \quad (16)$$

Mathematically, the d-FFE (14)~(16) follows the definition of distributed-order fractional-derivative equations (Chechkin et al., 2002; Luchko, 2011; Naber, 2004), which were proposed to capture time-dependent dynamics (although they have not been checked against real-world hydrologic processes). The smaller of the two indexes  $\alpha_1$  and  $\alpha_2$  dominates the late-time flow behavior, such as the late-time water retention missed by the single-index t-FFE (12). When the indexes  $\alpha_1 = 1$  and  $\alpha_2 = 1$  (i.e., without memory impact in any zones), models (14) and (15) reduce to the standard MRMT flow model with a single mass-transfer rate, such as Equations 5 and 6 in Silva et al. (2009). When  $\beta = 1$  (i.e., without separation of mobile/immobile zones), model (14) reduces to the single-index t-FFE (12).

Boundary and initial conditions for the three hydraulic heads listed above can be written as:

$$H_k(x = x_l, t) = H_l, \quad (17a)$$

$$H_k(x = x_r, t) = H_r, \quad (17b)$$

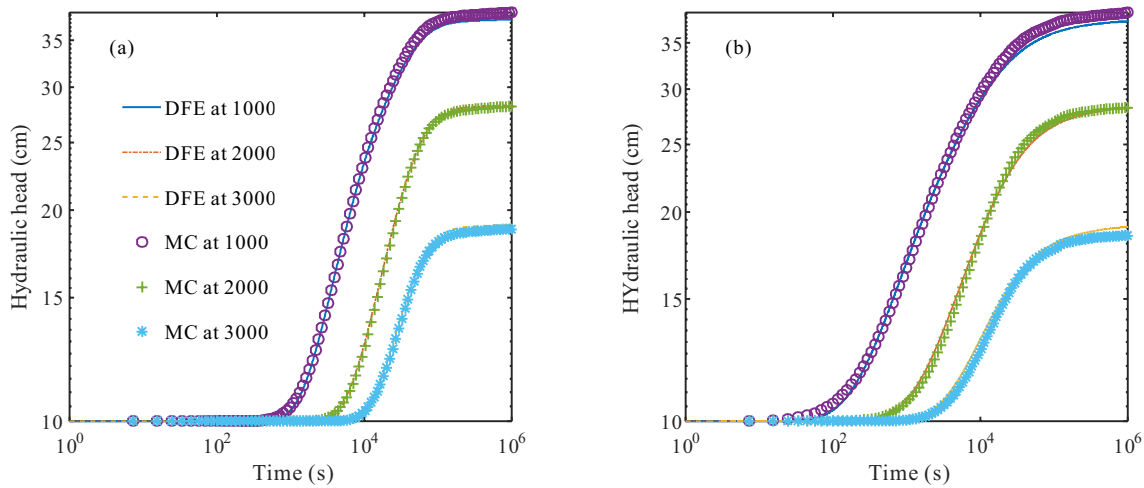


**Figure 8.** The transient piezometric head at three control planes (located at  $x = 1,000, 2,000,$  and  $3,000$  cm) for scenario 3 (left) and scenario 6 (right) in a log-log plot: Monte Carlo simulations (symbols) versus the distributed-order fractional flow equation (d-FFE) results (lines).

$$H_k(x, t = 0) = H_r, \quad (17c)$$

where the suffix  $k = m, im,$  or  $tot,$  representing the mobile, immobile, or total phase, respectively.

Taking the Laplace transform of Equation 15 ( $t \rightarrow \tau$ ), one obtains:

$$\tilde{H}_{im} = \frac{T}{\tau^{\alpha_2} + T} \tilde{H}_m + \frac{\tau^{\alpha_2 - 1}}{\tau^{\alpha_2} + T} H^0, \quad (18)$$

where  $T = K_{im}/S_s$  denotes the diffusion coefficient for water pressure, and  $H^0$  denotes the initial hydraulic head of the immobile zone. Inserting Equation 18 into the Laplace transform of Equation 14, taking the inverse Laplace transform, and considering the fact that  $T(1 - \beta)/\beta$  is small, we obtain the solution for the hydraulic head in the mobile phase:

$$H_m(x, t) = H_r + \Delta H \frac{x}{L} - \Delta H \frac{2}{\pi} \sum_{n=1}^{\infty} \frac{1}{n} \sin\left(\frac{n\pi}{L} x\right) \cdot E_{\alpha} \left( -\frac{K_e}{S_s} \frac{n^2 \pi^2}{L^2} t^{\alpha_1} \right), \quad (19)$$

where  $\Delta H = H_l - H_r$ .

Inserting Equation 18 into the Laplace transform of Equation 16 yields:

$$\tilde{H}_{tot} = \frac{\beta \tau^{\alpha_2} + T}{\tau^{\alpha_2} + T} \tilde{H}_m + \frac{(1 - \beta) \tau^{\alpha_2 - 1}}{\tau^{\alpha_2} + T} H^0. \quad (20)$$

Equation 20 is consistent with the known conditions listed below. When  $\beta = 1$ , Equation 20 shows that  $H_{tot} = H_m$  and all the domains are mobile, showing that the d-FFE (14) and (15) reduce to the single-index t-FFE (12), as expected. In addition, for the case of  $T = 0$  (i.e., impermeable deposits comprising the immobile zone), Equation 18 reduces to  $H_{im} = H^0$ , consistent with no head change in the impermeable domain, and Equation 20 reduces to  $H_{tot} = \beta H_m + (1 - \beta)H^0 = \beta H_m + (1 - \beta)H_{im}$ , which is consistent with the total head defined by Equation 16. When  $T$  is non-zero and the time  $t \rightarrow \infty$  (corresponding to  $\tau \rightarrow 0$ ), Equation 18 shows the trend  $H_{im} \rightarrow H_m$  and Equation 19 predicts a linear gradient of head from  $H_l$  at  $x_l$  to  $H_r$  at  $x_r$ , and Equation 20 leads to  $H_{tot} \rightarrow H_m$ . Hence, Equation 20 defines the temporally nonlocal relationship between  $H_{tot}$  and  $H_m$ . When  $\alpha_2 = 1$ , the memory function is an exponential function representing weak retention in flow, and when  $\alpha_2 < 1$ , the memory function is a power law function capturing strong retention in water flow.

Applications show that the d-FFE (14)~(16) can capture the overall trend of the Monte Carlo solutions of the water BTC (Figure 8). The best-fit model parameters have the following values: for scenario 3,  $\alpha_1 = 0.95$ ,  $\alpha_2 = 0.13$ ,  $\beta = 0.9$ , and  $T = 0.04 \text{ cm}^2 \text{ s}^{-\alpha_2}$ ; and for scenario 6,  $\alpha_1 = 0.71$ ,  $\alpha_2 = 0.11$ ,  $\beta = 0.92$ , and  $T = 0.04 \text{ cm}^2 \text{ s}^{-\alpha_2}$ .

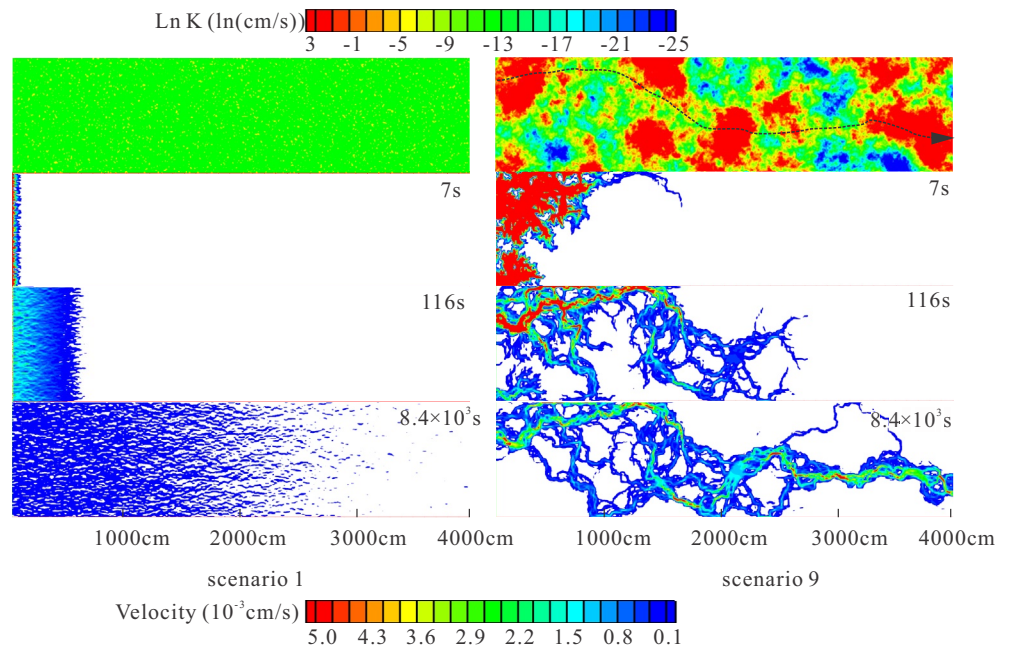


**Figure 9.** Conductivity field (top row) and the simulated streamlines (three bottom rows) for realization 1 in scenario 1 (left) and scenario 9 (right). The dotted line (in the upper right plot) connecting high- $K$  areas shows the main pathway of water.

In Appendix B, we explain and validate further how the d-FFE (14)~(16) can distinguish flow retention at different times, especially the intermediate and late times. We also conduct detailed model comparison in Appendix C, where results show that the d-FFE (14)~(16) (with four fitting parameters:  $\alpha_1$ ,  $\alpha_2$ ,  $\beta$ , and  $K_{im}$ ) is superior to the s-FFE (2) and the general MRMT flow model in capturing the overall pattern of the water BTCs.

## 5. Discussion

### 5.1. Impact of High- $K$ on Early Arrivals in Water BTC

The simulated velocities shown in Figure 3 imply that the flow network consisting of high- $K$  channels plays a key role in the transient flow process. Both the variance and correlation range of  $K$  can affect properties of the preferential pathways and therefore affect early arrivals of water parcels. On one hand, a small variance of  $\text{Ln}(K)$  produces a relatively uniform flow velocity without apparent bifurcations. With an increasing variance of  $\text{Ln}(K)$ , the flow network exhibits densely braided channels (if the correlation range of  $K$  is short, such as in scenario 3) or fewer dominant meandering channels (if  $K$  is highly correlated, such as in scenario 9). The broader distribution of high- $K$  materials enhances the tortuosity of the flow network. On the other hand, a larger correlation range of  $K$  can result in wider channels with more direct connections between the inlet and outlet filled with fast-flowing water. However, if the variation of  $\text{Ln}(K)$  is below a threshold (which is 0.1 in this study; see Section 2.2), the impact of correlation range on the flow network is negligible, due to the relatively uniform  $K$ . Therefore, the correlation range of  $K$  acts as a secondary factor in controlling flow patterns as compared to the variance of  $K$ .

Time-dependent streamlines (at relatively early times) for scenarios 1 and 9 are shown in Figure 9. When the  $K$  of the porous medium has a large variance and strong correlation range, water tends to move downstream along multiple meandering preferential pathways. These preferential pathways grow in space with the downstream motion of the water wave, and the water flow velocity can significantly change with time even at the same position in the channel. The channel can bifurcate (to bypass low-permeability zones) or converge (due to spatial connectivity of high-permeability zones), while the average thickness of major



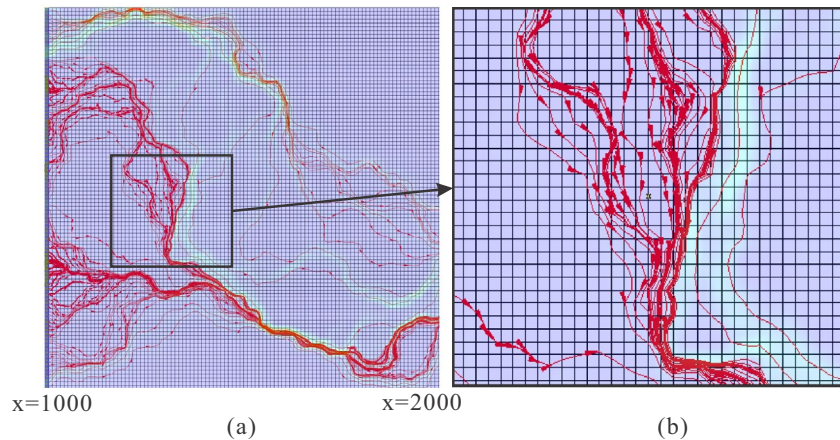


**Figure 10.** Streamlines (denoted by the red lines) for realization #1 in scenario 9, at  $t = 1,000$  s. Plot (b) shows the content in the rectangle depicted in (a). Note that the “pale green” lines represent the dense streamlines with relatively high velocities.

flow channels may not significantly change with distance, due likely to the stationary heterogeneity of the medium.

### 5.2. Impact of Low-K on Transient Flow

At intermediate times, the transverse differential flow paths due to the low- $K$  zones surrounding the high- $K$  channels or mixed with high- $K$  areas generate a wide distribution of prolonged arrival times for water parcels, which delays the propagation of hydraulic pressure. With the increase in the  $K$ -variance and  $K$ -correlation range, there are larger continuous areas of low- $K$  materials that impede longitudinal water movement and increase the transverse flow velocity (for example, see Figure 10). The low- $K$  materials, therefore, are responsible for the delayed flow at the intermediate stage. When the variance of  $K$  is small,  $K$  is relatively uniform, which cannot significantly intercept incoming water, resulting in piston flow. This may also explain why there exists a threshold of  $K$ -variance, which triggers complex flow dynamics.

At late times, “islands” consisting of discrete low- $K$  cells begin to significantly affect flow dynamics (Figure 11). For the purposes of this discussion, islands are defined as cells where the increase of the hydraulic head is no more than 1 cm (resulting in a large head different ( $>30.0$  cm) with the surrounding cells) after time  $t = 10^5$  s. The volumetric proportion of the islands is low (typically  $<10\%$ ). Values of  $K$  for these islands vary from  $10^{-10}$  cm/s to  $10^{-7}$  cm/s, representing silt/clay deposits

(the typical  $K$  ranges for silt and clay are  $10^{-11}$ – $10^{-5}$  cm/s (Domenico & Schwartz, 1990)). Due to the extremely low  $K$ , these discrete areas do not allow water to penetrate easily, and hence the hydraulic head increases very slowly. At late times when the hydraulic head in the surrounding areas has stabilized, the island remains at a low hydraulic head (close to its initial head) and hence is surrounded by a relatively high hydraulic head gradient. It can take an extremely long time (e.g.,  $>10^7$  s) for the head to rise in the island, and for the whole system to reach stability (Figure 12). This effect explains the enhanced retention behavior at late times for scenarios 3 and 6, where the average hydraulic head at each control plane arrives slowly during the late period of  $10^5$ – $10^6$  s. This time-dependent behavior cannot be captured by the single-index t-FFE (12), which assumes a stationary memory function (meaning that the memory function (10) has a fixed exponent  $\gamma$ ). As demonstrated in Section 4, stochastic models with multiple indexes, such as the d-FFE (14)–(16), are needed to capture the strong impact of both high- $K$  and low- $K$  materials on transient flow dynamics.

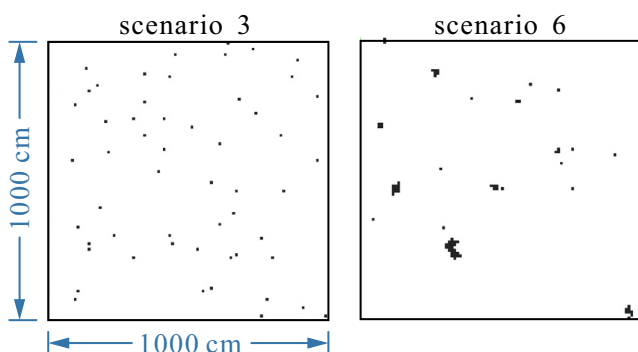


**Figure 11.** “Islands” consisting of low- $K$  zones for scenario 3 (left) and scenario 6 (right). Here the islands (represented by the dots) are defined as cells where the increase of the hydraulic head is no more than 1 cm (resulting in a large head different ( $>30.0$  cm) with the surrounding cells) after time  $t = 10^5$  s.

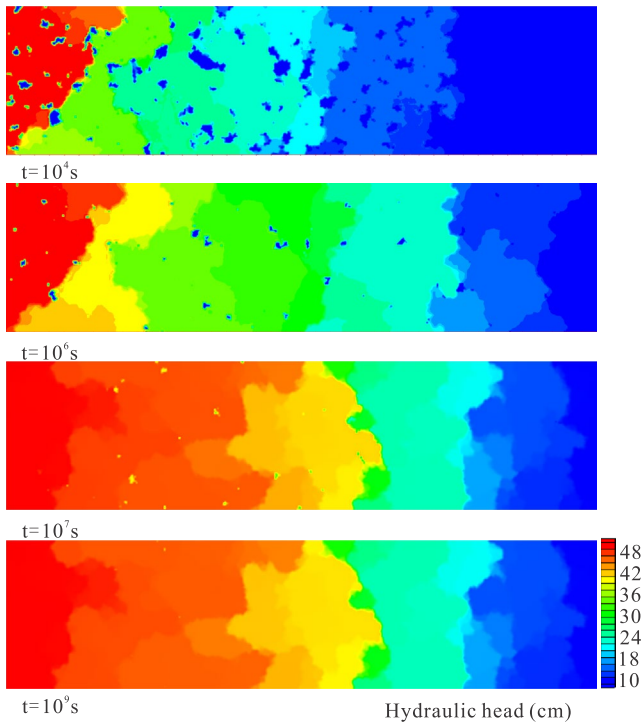


**Figure 12.** The evolution of the Monte Carlo simulation of the hydraulic head contour for realization 1 of scenario 6. The domain size is 4,000 cm by 1,000 cm along the longitudinal and transverse directions, respectively. The area of “islands,” denoted by the low- $K$  blocks with relatively lower hydraulic head than the surrounding cells, shrinks with time. The domain size shown in this plot is 4,000 cm by 1,000 cm along the longitudinal and transverse directions, respectively.

Therefore, the low- $K$  zones provide a possible mechanism to generate temporally non-Darcian flow and non-Fickian propagation of water pressure at late times. Water flux with the delayed transfer of water pressure due to low- $K$  islands violates the standard Darcy’s law-based flow equation (with constant parameters) which is a classical (Fickian) diffusion equation. This mechanism is more like a sub-diffusive transfer of water pressure, similar to the concept of “sub-diffusive flow in a composite medium” proposed first by Raghavan and Chen (2020), which is opposite to the super-diffusive flow defined by the s-FFE (2).

### 5.3. Non-Darcian Flow and Non-Fickian Pressure Propagation

We did not find the non-Darcian flow defined by Equation 1 or the resultant non-Fickian pressure propagation due to the non-Darcian flow (1) in the stochastic  $K$  fields built for this study. Equation 1 usually describes turbulent flow, inertial flow, or other high velocity flow, which causes super-diffusive non-Fickian spreading of water pressure. Super-diffusion of the pressure front is precluded in this study by the finite number of preferential flow paths, implying that the PDF of the longitudinal seepage velocity cannot be as heavy as the  $\alpha$ -stable density (see further discussion and model comparison in Appendix C). The same conclusion was found by Zhang et al. (2014) when modeling flow and transport in thousands of alluvial aquifer/aquitard systems represented by high-resolution hydro-facies models. However, it is possible that the spherical semi-variogram model used by this study cannot capture power-law distributed and correlated  $K$  fields. A power-law PDF for velocity is one of the core conditions to generate super-diffusive displacement of water parcels. Several recent studies showed that the (well-connected) high  $K$  is needed in the Monte Carlo models to reproduce super-diffusion for solutes observed at the MADE aquifer (Bianchi & Zheng, 2016; Yin et al., 2020), where the non-Darcian flow (1) might exist. This assumption may be addressed in a future study.

Sub-diffusive non-Fickian propagation of water pressure in this study, characterized by the elongated water BTCs, is caused by water trapping or transverse retention at intermediate times (due to the differential transverse flow paths and the corresponding random travel periods, as discussed in Section 3.2) and water retention at late times (due to the long-term mass exchange between the high- $K$  and low- $K$  islands, as discussed in Section 5.2). This is analogous to the well-documented anomalous transport for conservative solutes in heterogeneous geological media: non-Fickian diffusive flux analogous to model (1) causes super-diffusive non-Fickian transport of solutes, while the commonly observed sub-diffusive non-Fickian transport is caused by solute retention where solute diffusion in the operational time remains Fickian (Zhang et al., 2020).

Notably, non-Darcian flow and non-Fickian pressure propagation may be related. As shown by Equation A5, although there is no spatially nonlocal flow in our random  $K$  fields, water retention/delay due to low- $K$  materials may be characterized by the time-nonlocal non-Darcian flow equation expressed by Equation A5. To distinguish the hydrogeological mechanisms underlying Equations 1 and 5, we call Equation 1 the “spatially non-Darcian flow equation” and Equation A5 the “temporally non-Darcian flow equation.” In this study, temporally non-Darcian flow is more likely than spatially non-Darcian flow as a result of sub-diffusive non-Fickian pressure propagation.

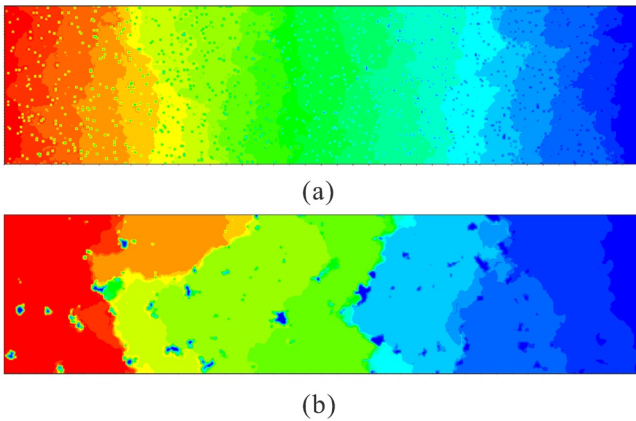


**Figure 13.** Sensitivity analysis: Monte Carlo simulations of the hydraulic head contour at time  $1 \times 10^5$  s for realization 1 of scenario 3 (a), and realization 1 of scenario 6 (b), when the lower bound (i.e., the minimum) of the hydraulic conductivity  $K_{\min} = 1 \times 10^{-9}$  cm/s. The domain size shown in this plot is 4,000 cm by 1,000 cm along the longitudinal and transverse directions, respectively. The color scale is the same as that shown in Figure 12.

#### 5.4. Model Parameter Estimation and Impact of K-Fields on Water Dynamics

Here we provide an empirical estimate of the fractional index  $\alpha$  using the variance of  $\ln(K)$  (denoted as  $C$ ) and/or the correlation range  $R$ . The analyses shown above reveal that both the variance and correlation range of  $K$  are positively correlated with  $\alpha$ . Given the best-fit results in Section 3, we obtain an empirical formula to predict the fractional index  $\alpha$  in the t-FFE (12):

$$\alpha = 1 - \left[ 0.095 \ln(R) + 0.09 C^{0.699} - 0.322 \right]. \quad (21)$$

To test the prediction (21), we then set a new scenario with the correlation range,  $R$ , being 300 cm and the  $\ln(K)$  variance,  $C$ , being 5. The predicted  $\alpha$  using Equation 12 is 0.72, which is close to the best-fit value (0.71). For the d-FFE (14)~(16), the empirical formula takes a similar form:

$$\alpha_1 = 1 - \left[ 0.082 \ln(R) + 0.09 C^{0.699} - 0.365 \right]. \quad (22)$$

We also evaluated the impact of  $K$ -fields on water dynamics, by first evaluating the influence of the lower bound of  $K$  (denoted as  $K_{\min}$  here) on the late-time flow. For the previous  $K$  fields, all values below a threshold value were set to the threshold value, and the flow models were rerun. The results show that, with a relatively large  $K_{\min}$  (equal to  $1 \times 10^{-9}$  cm/s), the islands persist in scenarios 3 and 6 at a late time  $t = 10^5$  s (Figure 13).

These islands, however, will then disappear earlier (at  $t = 10^6$  s) than those in Section 3 (with a much smaller  $K_{\min}$ ), since water can now enter the islands more quickly. Hence, increasing the lower bound of the hydraulic conductivity does not prevent the appearance of islands, but shortens their duration.

We also test the sensitivity of flow dynamics to the hydraulic conductivity at the peak  $K$  value of the distribution, denoted as  $K_{\text{peak}}$  here (which represents the mode of  $\ln(K)$ ). Scenario 9 is selected as the target medium. In the Monte Carlo simulations shown in Section 3,  $K_{\text{peak}}$  is  $3.0 \times 10^{-3}$  cm/s, and the best-fit parameters for the t-FFE (12) are:  $K_e = 1.7 \times 10^{-1}$  cm/s and  $\alpha = 0.50$  for scenario 9. When  $K_{\text{peak}}$  decreases to  $1.0 \times 10^{-3}$  cm/s, Monte Carlo simulations show that the water BTC for scenario 9 exhibits a similar trend, although the overall arrival of water is now delayed (Figure 14a). The best-fit parameters using the t-FFE (12) are as follows:  $K_e = 8.0 \times 10^{-2}$  cm/s, and  $\alpha = 0.53$ . When  $K_{\text{peak}}$  increases to  $1.0 \times 10^{-2}$  cm/s, the resultant water BTC shifts toward younger ages which can be fitted by the t-FFE (12) with parameters  $K_e = 2.7 \times 10^{-1}$  cm/s and  $\alpha = 0.53$  (Figure 14b). Therefore, the scale index  $\alpha$  is not sensitive to  $K_{\text{peak}}$ , while the effective conductivity  $K_e$  increases with an increasing  $K_{\text{peak}}$ . This result is consistent with expectations.

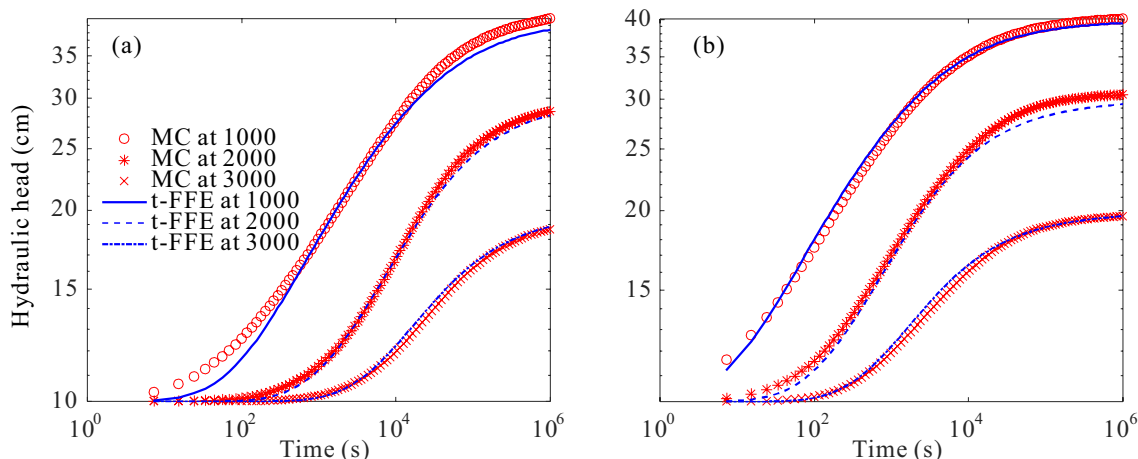


**Figure 14.** Sensitivity analysis: the transient piezometric head at three control planes (located at  $x = 1,000, 2,000,$  and  $3,000$  cm, respectively) for scenario 9 in a log-log plot with the peak PDF of  $K = 1.0 \times 10^{-3}$  cm/s (a) and  $1.0 \times 10^{-2}$  cm/s (b): Monte Carlo simulations (symbols) versus the t-FFE (12) results (lines).

On one hand, the internal architecture of the medium, which is mainly affected by the variance and correlation range of  $K$ , controls the overall temporal evolution of groundwater flow, which can be captured by the index  $\alpha$ . Hence, it is not the mode of  $K$  (or  $\text{Ln}(K)$ ), but the distribution of  $K$  that significantly affects the scale index  $\alpha$ . On the other hand,  $K_{\text{peak}}$  affects the overall permeability, and therefore controls the effective conductivity  $K_e$ .

It is also noteworthy that the physical/mathematical meaning of the index  $\alpha$  is clear:  $\alpha$  is the (absolute) exponent of the power-law PDF of the random operational time for water parcels in the porous medium. It is, however, not feasible to directly measure  $\alpha$ , because one cannot monitor each water parcel at present. This work provides guidance to empirically approximate this parameter based on statistics of measurable sedimentary properties (see Equations 21 and 22).

### 5.5. Velocity Distributions and Pollutant Transport

The velocity distributions for all scenarios when the hydraulic heads stabilize are plotted in Figure 15. The resultant velocity PDFs have a narrow distribution for aquifers with a small variance and short correlation for  $K$ , including scenarios 1, 4, and 7. For these scenarios with weak heterogeneity, the velocities along the longitudinal direction slightly deviate from the mean (Figure 15a), while the transverse velocities fluctuate around zero (where the mean transverse velocity is zero) (Figure 15c). These narrow velocity PDFs explain the observed piston flow without the apparent flow retention in Figure 4.

With the increase of medium heterogeneity (characterized by a larger variance and longer correlation for  $K$ ), the longitudinal velocity PDF expands to include greater probabilities for both large velocities (along preferential flow paths) and small velocities. The skewness of the longitudinal velocity PDF increases with the increase in the medium heterogeneity, implying the presence of enhanced flow regions. The peak velocity decreases with the increase in the velocity PDF's skewness, to maintain a constant mean velocity (Figure 15a). The "small" longitudinal velocity can be negative, representing local reverse flow due likely to the sinuous flow channels and the existence of low- $K$  zones. Meanwhile, the transverse velocity PDF expands and remains symmetric (Figure 15c), as expected.

It is noteworthy that the leading tail of the longitudinal velocity PDFs, which represents large velocities, declines exponentially (Figure 15b), which is lighter than a power-law function (i.e., not strong enough to produce super-diffusive displacement for water parcels) and validates our hypothesis in Section 5.3. The velocity PDF may be qualitatively related to the time index  $\alpha$  in the t-FFE (12): a broader velocity PDF (for scenarios with a larger correlation range and variance for  $\text{Ln}(K)$ ) with a higher probability for low longitudinal velocities (including negative velocities) (such as scenarios 3, 6, and 9 shown in Figure 15a) and a wider range of transverse velocities (such as scenarios 3, 6, and 9 shown in Figure 15c) represents stronger flow retention, which can be captured by a smaller index  $\alpha$  in the t-FFE (12). The qualitative correlation (between  $\alpha$  and  $\text{Ln}(K)$  properties) provides the hydrogeological interpretation for the empirical Equations 21 and 22.

The PDFs for the longitudinal and transverse velocity depicted in Figure 15 are insufficient for pollutant transport analysis, because dynamics of pollutant transport depend on both the velocity and dispersion, as well as the spatial structure of velocities. For example, Monte Carlo simulations showed that sub-diffusion for conservative pollutant transport in heterogeneous porous media was dominated by molecular diffusion (Zhang et al., 2007). Properties of low-permeable deposits, such as their thicknesses, affect the strength of molecular diffusion and therefore can be linked to the index of sub-diffusion (Zhang et al., 2014). Several other studies did reveal the potential correlation between the power-law distributed, uncorrelated velocities and anomalous transport (e.g., Herrick et al., 2002; Dentz & Bolster, 2010), but they focused on super-diffusion. In addition, the transient flow condition considered in this study makes it more difficult (than the steady-state flow) to link the time-dependent velocity PDF to complex anomalous transport. Pollutant transport dynamics require a detailed evaluation, which are not the focus of the current study.

The main parameter  $\alpha$  in Equation 12, however, may reveal new, important information for pollutant transport. This study found that some water BTCs can be quantified by the t-FFE (12), which contains two parameters: the index  $\alpha$  and the effective hydraulic conductivity  $K_e^*$ . The main parameter  $\alpha$  differs from the time fractional index  $\gamma$  in the fractional-derivative model to define sub-diffusive transport:



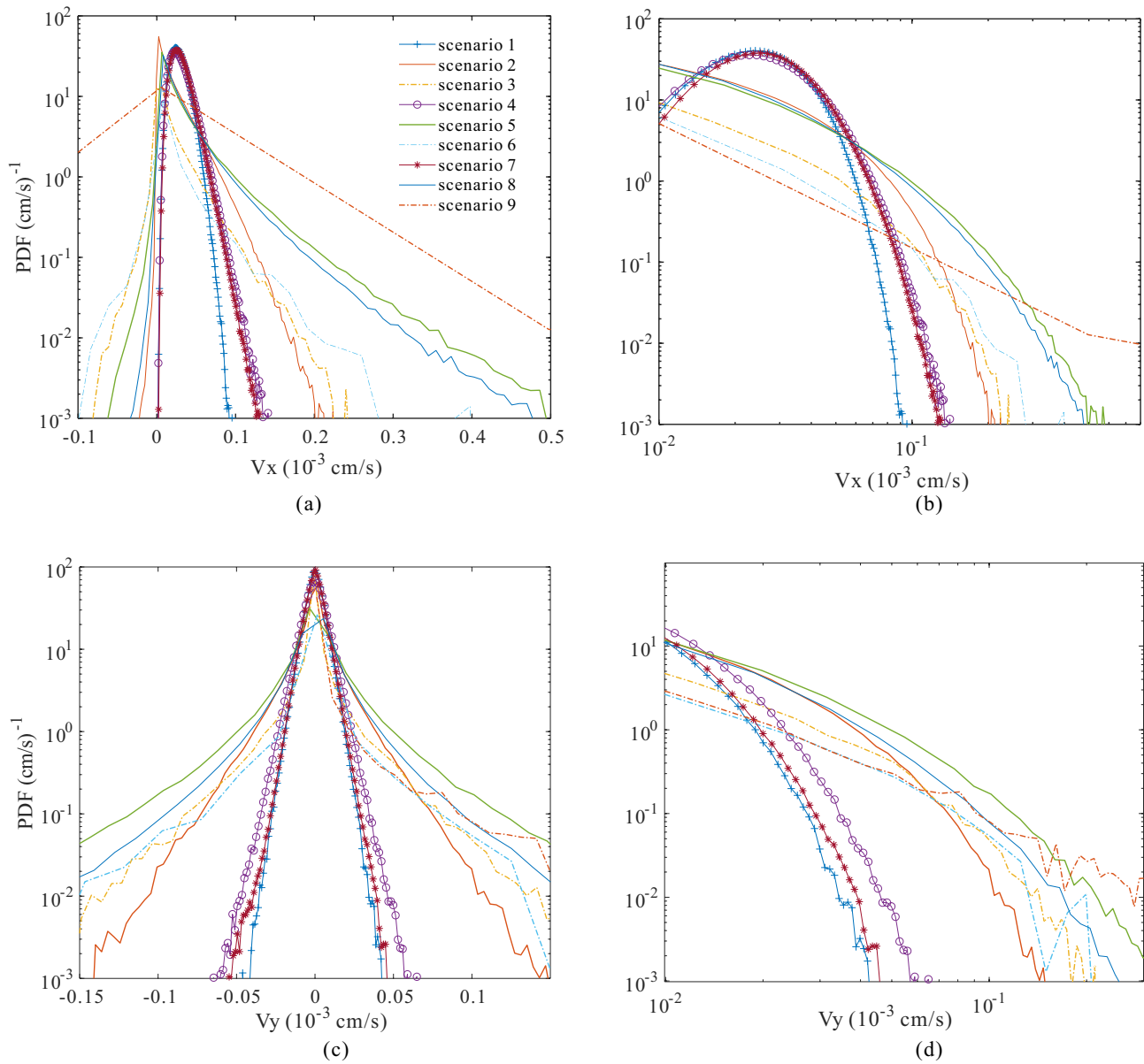


**Figure 15.** Probability density functions (probability density function) of Darcy velocity for scenarios 1~9 along the longitudinal ( $x$ ) direction (a) and the transverse ( $y$ ) direction (c) in a semi-log plot after stabilization of hydraulic head. Panels (b) and (d) are the log-log plots of (a) and (c), respectively, to emphasize the leading tail.

$\beta^* \frac{\partial^\gamma C}{\partial t^\gamma} = -V \frac{\partial C}{\partial x} + D^* \frac{\partial^2 C}{\partial x^2}$ . Forward and backward diffusion in low-permeability deposits is the main mechanism for sub-diffusive transport, while the blocking of water entry due to very low-permeability deposits is the major cause of groundwater retention. Although these two indexes ( $\alpha$  vs.  $\gamma$ ) characterize different mechanisms for different processes (water flow vs. pollutant transport), they are all related to properties of low-permeability deposits and therefore may be quantitatively related. For example, a smaller index  $\alpha$  in the water BTC due to more low- $K$  materials (i.e., a stronger groundwater retention process) may correspond to a smaller index  $\gamma$  in the pollutant BTC (i.e., a stronger solute retention). In addition, the applicability of the d-FFE (14)~(16) revealed that pollutant transport under transient flow is most likely a nonstationary process with a time-dependent index  $\gamma$ ; however, this inference requires further validation using similar Monte Carlo transport experiments.

### 5.6. Water BTC and Transport BTC

From the point of view of mathematical models, the water BTC calculated by this study relates to two special cases of transport BTCs. First, according to Darcy's law  $q = -K_e \frac{H_x(t) - H_l(t)}{L}$  (where  $K_e$  is the effective hydraulic conductivity,  $H_l(t)$  is the known head at the left boundary which is constant in this study, and  $L$  denotes the longitudinal distance from the left boundary to the control plane  $x$  where  $H_x(t)$  was calculated), the normalized water BTC,  $H_x(t)$ , may approximate the average (i.e., ensemble of all  $K$ -field realizations), normalized BTC for pollutants driven by pure advection with a continuous, stable source at the upstream boundary.

Second, the flow Equation 3a  $S_S \frac{\partial H}{\partial t} = \frac{\partial}{\partial x} \left[ K_{xx} \frac{\partial H}{\partial x} \right] + \frac{\partial}{\partial y} \left[ K_{yy} \frac{\partial H}{\partial y} \right]$  is mathematically similar to the transport equation  $\frac{\partial C}{\partial t} = \frac{\partial}{\partial x} \left[ D_{xx} \frac{\partial C}{\partial x} \right] + \frac{\partial}{\partial y} \left[ D_{yy} \frac{\partial C}{\partial y} \right]$  if  $D_{xx} = K_{xx}/S_S$  and  $D_{yy} = K_{yy}/S_S$ . Therefore, the water BTC can be regarded as a pure-diffusive transport BTC with a space-random dispersion coefficient which is proportional to the local hydraulic conductivity (i.e.,  $D_{xx} = K_{xx}/S_S$ , and  $D_{yy} = K_{yy}/S_S$ ).

## 6. Conclusions

This study explored and upscaled the full-range dynamics for transient flow through saturated porous media (characterized by a stationary variogram model for the  $K$  distribution). Monte Carlo simulations and stochastic model analysis were combined to explore the hydrogeological mechanism for flow dynamics, and then state-of-the-art, time-nonlocal physical models were developed. Four conclusions were drawn.

First, high- $K$  materials, which form interconnected preferential flow paths and affect the tortuosity, generate early arrivals of water parcels in downstream planes and dominate the early time dynamics of transient water flow, which however do not represent the super-diffusive pressure propagation assumed by the space-fractional, non-Darcian flow Equation 1. The preferential flow paths are enhanced with an increasing variance and correlation range of  $K$ . The resultant early tail in the water BTC is not as heavy as power-law, due to the limited number of flow channels. This behavior implies that the s-FFE (2) and others built upon Equation 1 tend to overestimate the early arrivals in transient flow, for the heterogeneous media considered in this study.

Second, the low- $K$  zones cause transient flow dynamics which have not been fully characterized before. Particularly, the low- $K$  zones exhibit different impacts on flow dynamics at intermediate and late times. At intermediate times, the low- $K$  zones surrounding the preferential flow paths can enhance the transverse movement of water, while at late times when hydraulic head in the relatively high- $K$  zones has stabilized, the low-permeability cells continue to resist the entry of water and therefore form islands where the local hydraulic head changes slowly from the initial value. Therefore, the low- $K$  zones are the major cause of groundwater retention with observable effects at intermediate times to late times.

Third, transient groundwater flow can be temporally non-Darcian and non-stationary (with sub-diffusive behavior in pressure propagation) in porous media with stationary heterogeneity (i.e., built with the stationary variogram model). This temporally non-Darcian groundwater flow is not the spatially non-Darcian flow assumed by previous work for super-diffusion. Sub-diffusive propagation of the pressure front explains the memory effect in groundwater flow, including delayed flow due to transverse movement at intermediate times and water retention at late times due to long-term mass exchange between high- $K$  and low- $K$  zones (i.e., "islands"). The nonstationary evolution of groundwater flow may affect groundwater management and remediation strategy.

Fourth, multi-index time-fractional derivative models can upscale transient groundwater flow over the full time-range. A single-index stochastic model such as the single-index t-FFE model (12) can capture retention at intermediate times in the water BTCs, but tends to overestimate the rate of increase of the head at late times, when "islands" of low- $K$  blocks resist changes of hydraulic head for an extremely long time. The same issue exists for the well-known and often-used MRMT model since the single-index t-FFE model is

equivalent to the MRMT model with upper-truncated rate coefficients. One major finding of this study is that the rate of decline of the pressure propagation at late times does not remain stable, but rather is time dependent. Hence, a multi-index stochastic model, such as the distributed-order fractional-derivative flow model developed in this study, should be used to capture the full time-range of water dynamics.

## Appendix A: Time Subordination Method to Derive the T-FFE and Temporally Non-Darcy's Law

The time-subordination approach, proposed first by Baeumer et al. (2001) to model anomalous transport for pollutants, has been applied to capture heavy-tailed responses from heterogeneous hillslopes (Harman et al., 2010; Zhang et al., 2017). Here we extended the approach to capture saturated flow in heterogeneous aquifers. Subordination is a mathematical method which transfers the clock time to operational time for random walkers (Feller, 1971), which are water parcels moving along streamlines in this study. The randomness in flow dynamics can be represented by the random time spent during each displacement for water parcels, which is the random operational time assumed by the subordination approach.

We randomize the operational time that a water parcel spends in motion in porous media, similar to the random operational time assumed by Harman et al. (2010) for a flow impulse spent in motion along a heterogeneous hillslope after precipitation. Following the definition in Harman et al. (2010) and Zhang et al. (2017), we also assume that the PDF of the operational time follows the  $\alpha$ -stable density, whose subordinator satisfies the following governing equation:

$$b \frac{\partial f(s, t)}{\partial t} = \frac{\partial^{1-\alpha}}{\partial t^{1-\alpha}} \frac{\partial f(s, t)}{\partial s}; f(s, 0) = \delta(s) \quad (\text{A1})$$

where the scale factor  $b = 1 [T^{\alpha-1}]$  is analogous to the factor  $\beta^*$  added to the model (12) for units conversion, and  $f [T^{-1}]$  is the density of the operational time.

The continuity equation of seepage flow takes the form:

$$S_s \frac{\partial h}{\partial t} = - \frac{\partial}{\partial x} q \quad (\text{A2})$$

Based on the time subordination described by Equation A1 and given any linear spatial operator defined on the right-hand side (RHS) of the continuity Equation A2, the time-subordinated flow has a hydraulic head that solves (Zhang et al., 2017):

$$b \frac{\partial \bar{H}(x, t)}{\partial t} = \frac{1}{S_s} \frac{\partial}{\partial x} \frac{\partial^{1-\alpha}}{\partial t^{1-\alpha}} q(x, t) = \frac{1}{S_s} \frac{\partial}{\partial x} \frac{\partial^{1-\alpha}}{\partial t^{1-\alpha}} \left[ K \frac{\partial \bar{H}(x, t)}{\partial x} \right], \quad (\text{A3})$$

which is a time subordinated flow equation with a general velocity  $q$  varying in space and time. Here the order of the time-fractional operator  $\partial^{1-\alpha}/\partial t^{1-\alpha}$  and the spatial operator  $\partial/\partial x$  cannot be changed unless for a constant, effective  $K^*$ , where the temporal operator on the RHS of Equation A3 can go to the left-hand side as an inverse, leading to a simplified, linear flow model:

$$b \frac{\partial^\alpha \bar{H}(x, t)}{\partial t^\alpha} = \frac{K^*}{S_s} \frac{\partial^2 \bar{H}(x, t)}{\partial x^2}, \quad (\text{A4})$$

which is mathematically equivalent to the t-FFE (12).

It is also noteworthy that the time subordinated flow Equation A3 defines a time-nonlocal, non-Darcian flow equation:

$$q^* = \frac{1}{b} \frac{\partial^{1-\alpha}}{\partial t^{1-\alpha}} q = \frac{1}{b} \frac{\partial^{1-\alpha}}{\partial t^{1-\alpha}} \left( K \frac{\partial \bar{H}}{\partial x} \right), \quad (\text{A5})$$

which applies the time fractional derivative (instead of the space fractional derivative used in the non-Darcy flow Equation 1 to capture non-Darcian flux due to both water retention (by low- $K$  materials discussed in Section 5.2 and water trapping or retaining (due to the transverse flow paths and the corresponding random travel periods during groundwater head evolution (see Sections 2 and 3.2).

## Appendix B: How Can the d-FFE (14)~(16) Capture Time-Dependent Flow Retention?

The core question to answer in this appendix is how the d-FFE (14)~(16) can distinguish flow retention at different times, especially the intermediate and late times, which exhibit different dynamics and cannot be fully captured by the single-index t-FFE (12). Equations 19 and 20 show that the hydraulic head in mobile, immobile, and total phases approach the same asymptote:  $H_r + \Delta H x/L$ , when  $t \rightarrow \infty$ . To evaluate the approaching rate for each phase, we calculate the head residual (which is the difference between the current hydraulic head and its asymptote) for the mobile, immobile, and total phases (denoted as  $R_m$ ,  $R_{im}$ , and  $R_{tot}$ , respectively) using the following formulas:

$$R_m = H_r + \Delta H \frac{x}{L} - H_m, \quad (B1a)$$

$$R_{im} = H_r + \Delta H \frac{x}{L} - H_{im}, \quad (B1b)$$

$$R_{tot} = H_r + \Delta H \frac{x}{L} - H_{tot}, \quad (B1c)$$

which also satisfy the original d-FFE (14)~(16):

$$\frac{\partial^{\alpha_1} R_m}{\partial t^{\alpha_1}} = \frac{K_e^*}{S_s} \frac{\partial^2 R_m}{\partial x^2} - \frac{1-\beta}{\beta} T (R_m - R_{im}), \quad (B2a)$$

$$\frac{\partial^{\alpha_2} R_{im}}{\partial t^{\alpha_2}} = T (R_m - R_{im}), \quad (B2b)$$

$$R_{tot} = \beta R_m + (1-\beta) R_{im}, \quad (B2c)$$

with different boundary and initial conditions:

$$R_k(x = x_l, t) = 0, \quad (B3a)$$

$$R_k(x = x_r, t) = 0, \quad (B3b)$$

$$R_k(x, t = 0) = -\Delta H \frac{x}{L}. \quad (B3c)$$

The solution for the head residual in the Laplace domain at a late time is:

$$\tilde{R}_m \Rightarrow \Delta H \frac{2}{\pi} \sum_{n=1}^{\infty} \frac{1}{n} \sin\left(\frac{n\pi}{L} x\right) \cdot \left(\tau^{\alpha_1-1}\right) \cdot \left(\frac{K_e^* n^2 \pi^2}{S_s L^2}\right)^{-1}, \quad (B4a)$$

$$\tilde{R}_{im} \Rightarrow \Delta H \frac{2}{\pi} \sum_{n=1}^{\infty} \frac{1}{n} \sin\left(\frac{n\pi}{L} x\right) \cdot \left[\left(\tau^{\alpha_1-1}\right) \cdot \left(\frac{K_e^* n^2 \pi^2}{S_s L^2}\right)^{-1} + \frac{\tau^{\alpha_2-1}}{T}\right], \quad (B4b)$$

$$\tilde{R}_{tot} \Rightarrow \Delta H \frac{2}{\pi} \sum_{n=1}^{\infty} \frac{1}{n} \sin\left(\frac{n\pi}{L} x\right) \cdot \left[\left(\tau^{\alpha_1-1}\right) \cdot \left(\frac{K_e^* n^2 \pi^2}{S_s L^2}\right)^{-1} + \frac{(1-\beta) \tau^{\alpha_2-1}}{T}\right], \quad (B4c)$$

Therefore, we obtain the approximated decline rate for the head residual at late times:

$$R_m \propto t^{-\alpha_1}, \quad (B5a)$$

$$R_{im} \propto t^{-\alpha^*}, \quad (B5b)$$

$$R_{tot} \propto t^{-\alpha^*}, \quad (B5c)$$

where  $\alpha^* = \min(\alpha_1, \alpha_2)$ . At late times, the hydraulic head in the mobile phase approaches its asymptote at a speed proportional to  $t^{-\alpha_1}$ , while the heads at the immobile and total phases grow at a speed of  $t^{-\alpha^*}$ . Hence, if  $\alpha_2 < \alpha_1$  (which is the case for this study), the flow retention becomes stronger at late times.

We checked the “actual” head residual for Scenario 3 and Scenario 6 (see Figure B1). Monte Carlo simulations show a power-law decline of the head residual in the total phase, and this rate changes with time: a



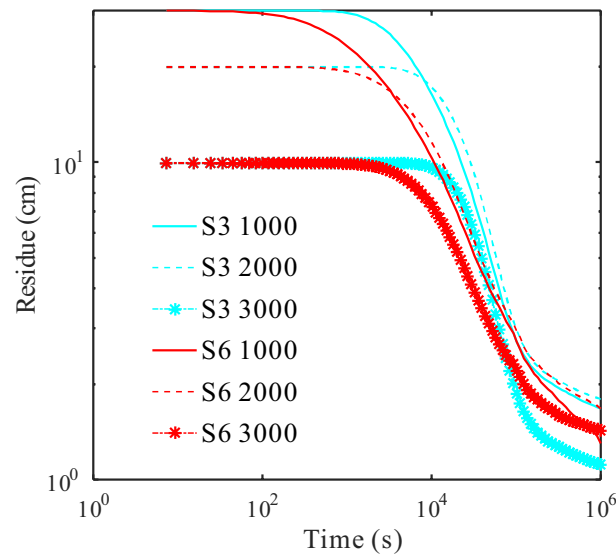


**Figure B1.** Monte Carlo simulation results: the transient residual of the hydraulic head in the total phase for scenario 3 and scenario 6 at various control planes ( $x = 1,000, 2,000, \text{ and } 3,000$  cm, respectively). In the legend, “S3” denotes scenario 3, and “S6” denotes scenario 6. Here the head residual is the difference between the current hydraulic head and its asymptote, which was calculated by Equation B1.

larger rate at intermediate time, followed by a smaller rate at very late time representing stronger retention (Figure B1). This behavior revealed by the numerical models is consistent with the analytical solution Equation B5.

### Appendix C: Model Comparison

Here we compare the d-FFE (14) and (15) with two other popular models related to fractional derivative models. First, we check the feasibility of the s-FFE (2) proposed by various researchers (Cloot & Botha, 2006; He, 1998; Mehdinejadiani et al., 2013), which can be written in the following form with an effective  $K$ :

$$S_s \frac{\partial H(x,t)}{\partial t} = K \frac{\partial^\eta H(x,t)}{\partial x^\eta}, \quad (\text{C1})$$

where the space index  $1 < \eta \leq 2$ . Application shows that the s-FFE (C1) does capture early arrivals, but the resultant hydraulic head distributes nonlinearly in space, which deviates significantly from the “real,” linear head distribution at late times (Figure C1). The hydraulic head described by (C1) stabilizes very quickly due to the super-diffusive motion of water parcels, and there is no water retention at any time. Hence, the space-fractional flow model (C1) is not appropriate to capture the real early time tail of the water BTC observed in this study. It is also noteworthy that the s-FFE (C1) describes a power-law distributed early arrival in the water BTC, due to the assumed super-diffusion. The actual early time tail of the water BTC, however, is not as heavy as power law, likely due to the limited number of preferential pathways (see Section 5.1 and Figure 3). A limited number of early arriving pulses cannot form a wide distribution of the water BTC as heavy as a power-law function. In addition, model (C1) or any fractional-derivative models built upon the space fractional flow Equation 1 cannot capture the late-time tailing of the water BTC identified in Section 5.2. One more example of the s-FFE (C1) is shown in Figure C2, where the water BTC simulated by the s-FFE (C1) exhibits a steeper slope and earlier arrivals than those simulated by the time fractional-derivative model (12), because the s-FFE (C1) captures super-diffusion only and excludes sub-diffusion characterized by apparent flow retention.

Second, we compare the d-FFE (14)~(16) with the MRMT model for water flow proposed by Silva et al. (2009). The MRMT model for flow with linear mass exchange between mobile and immobile phases,

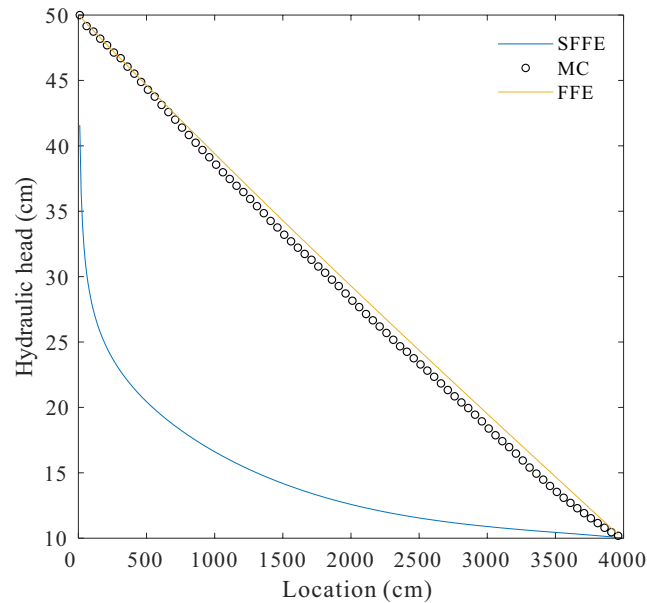


**Figure C1.** Comparison between the time and space fractional-derivative models: the spatial distribution of the hydraulic head at time  $t = 10^6$  s for Scenario 6. In the legend, “SFPE” denotes the space-fractional flow Equation 2 (here the spatial distribution of hydraulic head is the solution of the s-FPE (2) assuming non-Darcian flow (1) by fitting the Monte Carlo water BTC), “FPE” denotes the time-fractional flow Equation 12, and “MC” denotes the Monte Carlo result.

which is analogous to the well-known MRMT model for solute transport (Haggerty et al., 2000), takes the form (see Equations 1 and 2 in Silva et al. (2009)):

$$\beta S_m \frac{\partial h_m}{\partial t} + \sum_{j=1}^N \beta_j S_{im,j} \frac{\partial h_{im,j}}{\partial t} = -\frac{\partial}{\partial x} q, \quad (\text{C2a})$$

$$S_{im,j} \frac{\partial h_{im,j}}{\partial t} = \alpha_j (h_m - h_{im,j}), \quad j = 1, 2, \dots, N, \quad (\text{C2b})$$

where  $S_m$  and  $S_{im,j}$  [ $L^{-1}$ ] denote the specific storage coefficient in the mobile and the  $j$ th immobile zones, respectively;  $q$  [ $LT^{-1}$ ] is the water flux (assuming the longitudinal direction here for simplicity), and  $\alpha_j$  [ $T^{-1}$ ] denotes the  $j$ th rate coefficient which was defined as  $\alpha_j = \sigma_{im,j} K_{im,j}/L_{im,j}$  by Silva et al. (2009) (where  $\sigma_{im,j}$

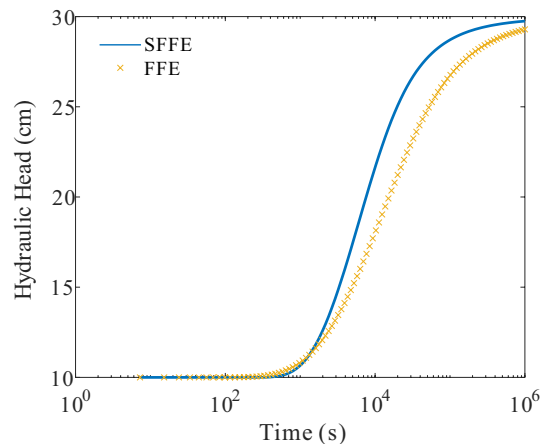


**Figure C2.** Further comparison between the time fractional-derivative model (“FPE”, model (12)) and the space fractional-derivative model (“SFPE”, model (2) or (C1)): the simulated water BTC for scenario 6 with a distance  $x = 200$  cm.

$[L^2L^{-3}]$  is the specific surface of the  $j$ th immobile zone,  $K_{im,j} [LT^{-1}]$  is the effective hydraulic conductivity for the  $j$ th immobile zone, and  $L_{im,j} [L]$  is the distance from the mobile zone to the  $j$ th immobile zone). In the Monte Carlo simulations conducted in this study, the storage coefficient was assumed to be constant.

According to Haggerty et al. (2000), hydraulic head in the immobile phase is the convolution of head in the mobile phase:

$$h_{im,j} = \alpha_j e^{-\alpha_j t} * h_m, \quad (C3)$$

with the overall memory function defined as  $\sum_{j=1}^N \beta_j \alpha_j e^{-\alpha_j t} / \beta$  (Haggerty et al., 2000). The symbol “\*” in (C3) denotes convolution. At a late time  $t \gg 1/\alpha_{\min}$  (where  $\alpha_{\min}$  denotes the minimum rate coefficient, and  $1/\alpha_{\min}$  represents the mean time for water parcels staying in the immobile zone with the slowest mass exchange rate), the mobile and immobile heads begin to stabilize.

There is no analytical solution for the general form of (C2), and hence we solve it numerically using an iterative approach with an implicit finite difference scheme. Extensive fitting exercises show that the late-time behavior of the water BTC cannot be captured with a single rate coefficient. For example, for scenario 9 at the distance of  $x = 1,000$  cm, the MRMT model (C2) with a single rate  $\alpha = 10^{-3} \text{ s}^{-1}$  overestimates the rate of increase of the “measured” hydraulic head after time  $t \gg 10^3$  s (because after  $1/\alpha$ , the immobile phase can no longer block the flow and the hydraulic head in the immobile phase begins to reach equilibrium) (Figure C3). We tested the single-rate mass transfer model (i.e.,  $N = 1$  in model (C2)) with many values of  $\alpha$ , and none of them could capture the overall trend of the water BTC (not shown here). Multiple rate coefficients are therefore needed to capture the time-dependent, enhanced water trapping behavior. For the example shown in Figure C3, at least four rate coefficients are needed, which may create challenges for applicability of the MRMT model (C2). Notably, this comparison revealed that more mass exchange rates are needed when (transient) water flows for a longer time in a single spatial region, because water samples more low-permeability zones with increasing time. This implies that transient water flow may not be a stationary process, requiring additional rate coefficients in the MRMT model. In other words, the classical MRMT model may not be efficient in capturing transient flow with non-stationary water retention, while the d-FFE (14)~(16) provides an efficient alternative to the classical MRMT to model this non-Darcian flow. This is a new capability provided by our model in comparison with the MRMT classical model.

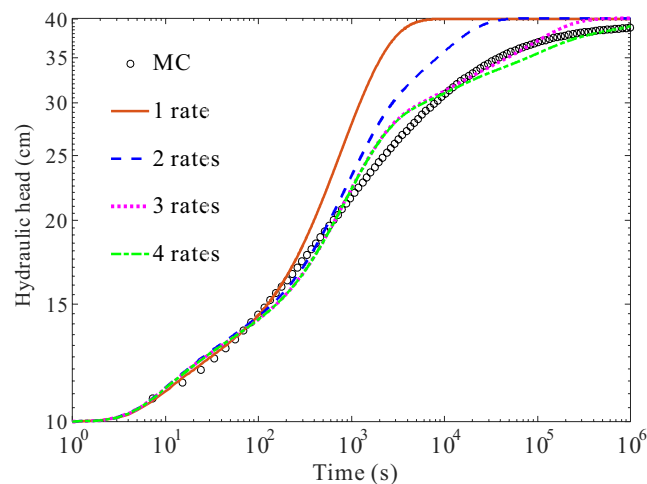


**Figure C3.** Best fit curves for the water BTC (for scenario 9 with a distance  $x = 100$  cm) using the multi-rate mass transfer model (C2). The legend shows the number of rate coefficients, the “1 rate” means a single rate coefficient ( $\alpha = 10^{-3} \text{ s}^{-1}$ ); the “2 rates” means two rate coefficients ( $\alpha_1 = 10^{-3} \text{ s}^{-1}$  and  $\alpha_2 = 10^{-4} \text{ s}^{-1}$ ); the “3 rates” model has three rates:  $\alpha_1 = 10^{-3} \text{ s}^{-1}$ ,  $\alpha_2 = 10^{-4} \text{ s}^{-1}$ , and  $\alpha_3 = 10^{-5} \text{ s}^{-1}$ ; and the “4 rates” model has four rates:  $\alpha_1 = 10^{-3} \text{ s}^{-1}$ ,  $\alpha_2 = 10^{-4} \text{ s}^{-1}$ ,  $\alpha_3 = 10^{-5} \text{ s}^{-1}$ , and  $\alpha_4 = 10^{-6} \text{ s}^{-1}$ .

## Appendix D: Model Limitations and Future Extension

Monte Carlo modeling in this study used a finite domain size, focused on the hydraulic head only, used a constant storage coefficient, and considered only 2D media (while realistic aquifers are always 3D). Although these four simplifications in numerical modeling were needed for an extensive quantification of transient groundwater head upscaling, each of them requires consideration before extending the results of this study. Therefore, specific cautions for interpreting results and logical future improvements are discussed below. Since none of these extensions are trivial, they may be the focus of future studies.

**Non-ergodic versus ergodic heterogeneous fields:** The limited domain size relative to the range of  $K$  can cause non-ergodic heterogeneous fields, resulting in artificial phenomena in the ensemble mean of the water BTC. On one hand, when the correlation range of  $K$  approaches the flow domain size, there is increased variability in the structure of the generated stochastic realizations of  $K$  fields, wherein the individual realizations (especially for scenarios 7~9 on the 4,000 cm scale with  $R$  equal to 500 cm, with one realization for each scenario shown by Figures 2g-2i) can deviate significantly from the ensemble mean behavior (such as the ensemble mean water BTCs depicted in Figures 4g-4i). This calls into question the meaning of an ensemble average water BTC (and the existence of any “effective hydraulic conductivity”) when averaging over a potentially non-ergodic  $K$  field. For example, tails in the apparent, mean water BTCs do not necessarily represent flow phenomena for individual realizations. Therefore, conclusions drawn from Figures 4g-4i may contain high uncertainty for the limited domain size used in this study. On the other hand, the scenarios with a shorter-range  $R$  (such as scenario 3) may reveal similar flow processes as the scenarios with a longer-range  $R$  (i.e., scenario 9, with the same semi-variogram model (except for  $R$ ) and  $K$  statistics) at a longer travel distance. This is because scenario 9 produces the same structure, but in essence with increasing magnification, compared to scenario 3. For example, the overall pattern of the Monte Carlo approach derived water BTC for scenario 3 ( $R = 10$  cm) at  $x = 500$  cm may look similar to that for scenario 9 ( $R = 500$  cm) at  $x = 500 \times (500/10) = 25,000$  cm, if scenario 9 is assigned a much lower general head gradient. Since all water BTCs in scenario 3 exhibit tailing and multi-stage characteristics, the same properties are expected for scenario 9, which can at least partially prove that the results shown in Figure 4 are reliable. A larger domain, however, is needed for scenario 9 in a future study to reduce the medium’s intrinsic uncertainty and check the hypothesis proposed here. Notably, the impact of the boundary condition on transient flow dynamics also needs further evaluation: this study assumed constant head boundaries to generate the overall longitudinal flow, but the constant heads at the upstream boundary may wipe out transverse changes in the hydraulic head at the boundary.

**Hydraulic head versus volumetric flux:** This study focused on the transient behavior of hydraulic head, since it represents groundwater information that can be directly measured in the field. Groundwater fluxes and water balance on the scales of aquifers or aquifer systems are often important when upscaling the hydraulic conductivity (such as from pumping tests), and the water flux is closely related to groundwater quantity and quality. The relevant question would be that if a representative effective  $K_e$  works for steady state for an individual realization (by matching the stable volumetric flux), does that effective  $K_e$  remain valid in the transient case (i.e., to properly reproduce the transient, volumetric flux profile)? The total transient flux across each control plane, therefore, should also be calculated and analyzed as the objective function in upscaling. Figure 4 and Table 1 showed that the effective  $K_e$  obtained for upscaling the steady-state flux only works for the transient flow in less heterogeneous media (with a small variance and correlation range for  $K$ ). It would be informative to systematically evaluate in a future study how the effective  $K_e$  obtained for upscaling the steady-state flux can change for transient flow.

**Fixed versus transient storage coefficient:** The Monte Carlo simulations of transient flow assumed a constant specific storage  $S_s$ , and the effective storage coefficient was also treated as constant when upscaling transient flow. The upscaled  $S_s$ , however, may increase with time in certain transient cases. With more heterogeneity and smaller  $K$  values in parts of the domain, because of less immediate access to storage changes in the tighter materials (as shown by the “islands” identified in the main text), the effective upscaled  $S_s$  may start out smaller than the average  $S_s$  and increase over time, as the full system gradually experiences storage changes. The time-dependent  $S_s$  may provide an alternative (and possibly easier) way (as opposed to the concept of memory function and the resultant t-FFE) to quantify the full-range of transient flow dynamics. This hypothesis remains an open research question.

2D versus 3D porous media: This study provides a simplified, planar view of 3D media. If a 2D porous medium is extended to 3D, the water BTC may exhibit different behaviors, especially the early and/or late time tailing. For example, a 3D medium will have more preferential pathways than a 2D medium with the same variance and correlation scale for  $K$ . Because water can now bypass low-permeability blocks via the third dimension, the effective hydraulic conductivity will be larger (and probably be easier to approximate using for example the arithmetic mean), resulting in earlier arrivals. Meanwhile, some water parcels may travel a greater distance due to longer and more sinuous flow paths in 3D, resulting in a heavier late-time tail in the water BTC. Systematic Monte Carlo analysis of 3D domains is needed in a future study to check the hypotheses mentioned above.

## Data Availability Statement

Data are available here [https://www.researchgate.net/publication/353368534\\_Data\\_of\\_Time-Fractional\\_Flow\\_Equations\\_t-FFEs\\_to\\_Upscale\\_Transient\\_Groundwater\\_Flow\\_Characterized\\_by\\_Temporally-Non-Darcian\\_Flow\\_Due\\_to\\_Medium\\_Heterogeneity](https://www.researchgate.net/publication/353368534_Data_of_Time-Fractional_Flow_Equations_t-FFEs_to_Upscale_Transient_Groundwater_Flow_Characterized_by_Temporally-Non-Darcian_Flow_Due_to_Medium_Heterogeneity).

## Acknowledgments

Yuan Xia was partially supported by the National Natural Science Foundation of China (under grant 41931292) and Collaborative Innovation Center for Water Pollution Control and Water Safety in Karst Area. Christopher T. Green was supported by the U.S. Geological Survey Water Mission Area. Yong Zhang was partially supported by the Alabama Center of Excellence (ALCoE). Graham E. Fogg was partially supported by the University of California, Davis, Agricultural Experiment Station Project CA-D-LAW-6036-H. This paper does not necessarily reflect the view of the funding agencies, except for the U.S. Geological Survey. Any use of trade, firm, or product names is for descriptive purposes only and does not imply endorsement by the U.S. Government.

## References

- Baeumer, B., Meerschaert, M. M., Benson, D. A., & Wheatcraft, S. W. (2001). Subordinated advection-dispersion equation for contaminant transport. *Water Resources Research*, 37(6), 1543–1550. <https://doi.org/10.1029/2000WR900409>
- Bear, J. (1978). *Hydraulics of groundwater*. McGraw-Hill.
- Bellin, A., Fiori, A., & Dagan, G. (2020). Equivalent and effective conductivities of heterogeneous aquifers for steady source flow, with illustration for hydraulic tomography. *Advances in Water Resources*, 142, 103632. <https://doi.org/10.1016/j.advwatres.2020.103632>
- Bianchi, M., & Zheng, C. M. (2016). A lithofacies approach for modeling non-Fickian solute transport in a heterogeneous alluvial aquifer. *Water Resources Research*, 52(1), 552–565. <https://doi.org/10.1002/2015WR018186>
- Cai, J., You, L., Hu, X., Wang, J., & Peng, R. (2012). Prediction of effective permeability in porous media based on spontaneous imbibition effect. *International Journal of Modern Physics C*, 23(7), 1250054. <https://doi.org/10.1142/s0129183112500544>
- Chechkin, A. V., Gorenflo, R., & Sokolov, I. M. (2002). Retarding subdiffusion and accelerating superdiffusion governed by distributed-order fractional diffusion equations. *Physical Review E*, 66(4), 046129. <https://doi.org/10.1103/physreve.66.046129>
- Cirpka, O. A., & Valocchi, A. J. (2016). Debates-Stochastic subsurface hydrology from theory to practice: Does stochastic subsurface hydrology help solving practical problems of contaminant hydrogeology? *Water Resources Research*, 52(12), 9218–9227. <https://doi.org/10.1002/2016wr019087>
- Clout, A., & Botha, J. F. (2006). A generalized groundwater flow equation using the concept of non-integer order derivatives. *Water SA*, 32(1), 1–7.
- Colechio, I., Boschian, A., Otero, A. D., & Noetinger, B. (2020). On the multiscale characterization of effective hydraulic conductivity in random heterogeneous media: A historical survey and some new perspectives. *Advances in Water Resources*, 140, 103594. <https://doi.org/10.1016/j.advwatres.2020.103594>
- Cortis, A., & Knudby, C. (2006). A continuous time random walk approach to transient flow in heterogeneous porous media. *Water Resources Research*, 42(10), 1–5. <https://doi.org/10.1029/2006WR005227>
- Cushman, J. H. (1997). *The physics of fluids in hierarchical porous media: Angstroms to miles* (p. 467.): Springer.
- Dagan, G. (1989). *Flow and transport in porous formations*: Springer-Verlag.
- Dagan, G. (1993). High-order correction of effective permeability of heterogeneous isotropic formations of log-normal conductivity distribution. *Transport in Porous Media*, 12, 279–290. <https://doi.org/10.1007/bf00624462>
- Dentz, M., & Bolster, D. (2010). Distribution- versus correlation-induced anomalous transport in quenched random velocity fields. *Physical Review Letters*, 105, 244301. <https://doi.org/10.1103/physrevlett.105.244301>
- Deseri, L., & Zingales, M. (2015). A mechanical picture of fractional-order Darcy equation. *Communications in Nonlinear Science and Numerical Simulation*, 20, 940–949. <https://doi.org/10.1016/j.cnsns.2014.06.021>
- Domenico, P. A., & Schwartz, F. W. (1990). *Physical and chemical hydrogeology*: John Wiley.
- Durlafsky, L. J. (2003). *Upscaling of geocellular Models for reservoir flow simulation: A Review of recent progress. 7th international forum on reservoir simulation*. <https://pdfs.semanticscholar.org/2cbc/4e1fb38620bde936b1f84b0e03cb39d9f91.pdf>
- Dykaar, B. B., & Kitanidis, P. K. (1992). Determination of the effective hydraulic conductivity for heterogeneous porous media using a numerical spectral approach, 1. Method. *Water Resources Research*, 28(4), 1155–1166. <https://doi.org/10.1029/91wr03084>
- Ergun, S. (1952). Fluid flow through packed columns. *Chemical Engineering Progress*, 48, 89–94.
- Feller, W. (1971). *An Introduction to Probability Theory and Its Applications* (2nd ed., Vol. 2): John Wiley.
- Fiori, A., Cvetkovic, V., Dagan, G., Attinger, S., Bellin, A., Dietrich, P., et al. (2016). Debates-Stochastic subsurface hydrology from theory to practice: The relevance of stochastic subsurface hydrology to practical problems of contaminant transport and remediation. What is characterization and stochastic theory good for? *Water Resources Research*, 52(12), 9228–9234. <https://doi.org/10.1002/2015wr017525>
- Fogg, G. E., & Zhang, Y. (2016). Debates-Stochastic subsurface hydrology from theory to practice: A geologic perspective. *Water Resources Research*, 52(12), 9235–9245. <https://doi.org/10.1002/2016wr019699>
- Garboczi, E. J. (1990). Permeability, diffusivity, and microstructural parameters: A critical review. *Cement and Concrete Research*, 20(4), 591–601. [https://doi.org/10.1016/0008-8846\(90\)90101-3](https://doi.org/10.1016/0008-8846(90)90101-3)
- Gelhar, L. W. (1993). *Stochastic subsurface hydrology*: Prentice Hall.
- Gelhar, L. W., & Axness, C. L. (1983). Three-dimensional stochastic analysis of macrodispersion in aquifers. *Water Resources Research*, 19(1), 161–180. <https://doi.org/10.1029/wr019i001p00161>



- Haggerty, R., McKenna, S. A., & Meigs, L. C. (2000). On the late-time behavior for tracer test breakthrough curves. *Water Resources Research*, 36(12), 3467–3479. <https://doi.org/10.1029/2000WR900214>
- Harbaugh, A. W. (2005). *Modflow-2005, the U.S. Geological Survey Modular Ground-Water Model—The Ground-Water Flow Process*. (Vol. 6-A16), (pp. 253). U.S. Geological Survey Techniques and Methods.
- Harman, C., Reeves, D. M., Baeumer, B., & Sivapalan, M. (2010). A subordinated kinematic wave equation for heavy-tailed flow responses from heterogeneous hillslopes. *Journal of Geophysical Research: Earth Surface*, 115, F00A08. <https://doi.org/10.1029/2009JF001273>
- He, J. H. (1998). Approximate analytical solution for seepage flow with fractional derivatives in porous media. *Computer Methods in Applied Mechanics and Engineering*, 167(1–2), 57–68. [https://doi.org/10.1016/S0045-7825\(98\)00108-X](https://doi.org/10.1016/S0045-7825(98)00108-X)
- Herrick, M. G., Benson, D. A., Meerschaert, M. M., & McCall, K. R. (2002). Hydraulic conductivity, velocity, and the order of the fractional dispersion derivative in a highly heterogeneous system. *Water Resources Research*, 38(11), 1227. <https://doi.org/10.1029/2001WR000914>
- Kendrick, A. K., Knight, R., Johnson, C. D., Liu, G. S., Knobbe, S., Hunt, R. J., & Butler, J. J., Jr. (2021). Assessment of NMR logging for estimating hydraulic conductivity in glacial aquifers. *Ground Water*, 59(1), 31–48. <https://doi.org/10.1111/gwat.13014>
- Knudby, C., Carrera, J., & Fogg, G. E. (2002). An empirical method for the evaluation of the equivalent conductivity of low-permeable matrices with high-permeable inclusions. In A. N. Findikakis (Ed.), *Proceedings of the International groundwater symposium, bridging the gap between measurement and modeling in heterogeneous media*: Lawrence Berkeley National Laboratory.
- Koltermann, C. E., & Gorelick, S. M. (1996). Heterogeneity in sedimentary deposits: A review of structure-imitating, process imitating, and descriptive approaches. *Water Resources Research*, 32, 2617–2658. <https://doi.org/10.1029/96wr00025>
- Li, C. R., Zheng, L., Zhang, X., & Chen, G. (2016). Flow and heat transfer of a generalized Maxwell fluid with modified fractional Fourier's law and Darcy's law. *Computers & Fluids*, 125, 25–38. <https://doi.org/10.1016/j.compfluid.2015.10.021>
- Luchko, Y. (2011). Initial-boundary-value problems for the generalized multi-term time-fractional diffusion equation. *Journal of Mathematical Analysis and Applications*, 374(2), 538–548. <https://doi.org/10.1016/j.jmaa.2010.08.048>
- Mehdinejadani, B., Naseri, A. A., Jafari, H., Ghanbarzadeh, A., & Baleanu, D. (2013). A mathematical model for simulation of a water table profile between two parallel subsurface drains using fractional derivatives. *Computers & Mathematics with Applications*, 66(5), 785–794. <https://doi.org/10.1016/j.camwa.2013.01.002>
- Metzler, R., & Klafter, J. (2000). The random walks guide to anomalous diffusion: A fractional dynamics approach. *Physics Reports*, 339(1), 1–77. [https://doi.org/10.1016/S0370-1573\(00\)00070-3](https://doi.org/10.1016/S0370-1573(00)00070-3)
- Metzler, R., & Klafter, J. (2004). The restaurant at the end of the random walk: Recent development in fractional dynamics of anomalous transport processes. *Journal of Physics A: Mathematical and General*, 37, R161–R208. <https://doi.org/10.1088/0305-4470/37/31/R01>
- Moghaddam, M. A. (2020). *Application and limitation of deep learning algorithms to hydrogeology - data driven approaches to understanding effective hydraulic conductivity, flux, and monitoring network design*. Dissertation: The University of Arizona.
- Municchi, F., & Icardi, M. (2020). Generalized multirate models for conjugate transfer in heterogeneous materials. *Physical Review Research*, 2, 013041. <https://doi.org/10.1103/physrevresearch.2.013041>
- Naber, M. (2004). Distributed order fractional sub-diffusion. *Fractals*, 12(01), 23–32. <https://doi.org/10.1142/S0218348X04002410>
- Obember, A. D. (2020). A fractional diffusion model for single-well simulation in geological media. *Journal of Petroleum Science and Engineering*, 191, 107162. <https://doi.org/10.1016/j.petrol.2020.107162>
- Pinczewski, W. V., & Paterson, L. (2002). Preface. *Transport in Porous Media*, 46, 117–117. <https://doi.org/10.1023/A:1017467430771>
- Qiu, P. T., Chen, Z. Q., Pu, H., & Zhu, J. (2019). Coupled effects of porosity and particle size on seepage properties of broken sandstone based on fractional flow equation. *Thermal Science*, 23(Suppl. 3), S943–S951. <https://doi.org/10.2298/tsci180602182q>
- Raghavan, R. (2011). Fractional derivatives: Application to transient flow. *Journal of Petroleum Science and Engineering*, 80, 7–13. <https://doi.org/10.1016/j.petrol.2011.10.003>
- Raghavan, R., & Chen, C. C. (2020). Subdiffusive flow in a composite medium with a communicating (absorbing) interface. *Oil & Gas Science and Technology - Rev. IFP Energies nouvelles*, 75(26), 26. <https://doi.org/10.2516/ogst/2020014>
- Rajaram, H. (2016). Debates-Stochastic subsurface hydrology from theory to practice: Introduction. *Water Resources Research*, 52(12), 9215–9217. <https://doi.org/10.1002/2016WR020066>
- Renard, P., & de Marsily, G. (1997). Calculating equivalent permeability: A review. *Advances in Water Resources*, 20(5–6), 253–278. [https://doi.org/10.1016/S0309-1708\(96\)00050-4](https://doi.org/10.1016/S0309-1708(96)00050-4)
- Rubin, Y., & Gómez-Hernández, J. J. (1990). A stochastic approach to the problem of upscaling of conductivity in disordered media: Theory and unconditional numerical simulations. *Water Resources Research*, 26(4), 691–701. <https://doi.org/10.1029/WR026i004p0691>
- Sanchez-Vila, X., & Fernández-García, D. (2016). Debates: Stochastic subsurface hydrology from theory to practice—Why stochastic modeling has not yet permeated into practitioners? *Water Resources Research*, 52(12), 9246–9258. <https://doi.org/10.1002/2016wr019302>
- Sanchez-Vila, X., Guadagnini, A., & Carrera, J. (2006). Representative hydraulic conductivities in saturated groundwater flow. *Reviews of Geophysics*, 44(3). <https://doi.org/10.1029/2005RG000169>
- Scheibe, T., & Yabusaki, S. (1998). Scaling of flow and transport behavior in heterogeneous groundwater systems. *Advances in Water Resources*, 22(3), 223–238. [https://doi.org/10.1016/S0309-1708\(98\)00014-1](https://doi.org/10.1016/S0309-1708(98)00014-1)
- Silva, O., Carrera, J., Dentz, M., Kumar, S., Alcolea, A., & Willmann, M. (2009). A general real-time formulation for multi-rate mass transfer problems. *Hydrology and Earth System Sciences*, 13, 1399–1411. <https://doi.org/10.5194/hess-13-1399-2009>
- Strangfeld, C. (2020). Determination of the diffusion coefficient and the hydraulic conductivity of porous media based on embedded humidity sensors. *Construction and Building Materials*, 263, 120092. <https://doi.org/10.1016/j.conbuildmat.2020.120092>
- Watanabe, H. (1982). Comment on Izbash's equation. *Journal of Hydrology*, 58(3–4), 389–397. <https://doi.org/10.1016/B978-0-408-10822-5.50020-8>
- Wei, D., Wang, Z., Pereira, J., & Gan, Y. (2021). Permeability of uniformly graded 3D printed granular media. *Geophysical Research Letters*, 48(5), e2020GL090728. <https://doi.org/10.1029/2020GL090728>
- Wen, X. H., & Gómez-Hernández, J. J. (1996). Upscaling hydraulic conductivities in heterogeneous media: An overview. *Journal of Hydrology*, 183(1–2), ix–xxxii. [https://doi.org/10.1016/S0022-1694\(96\)80030-8](https://doi.org/10.1016/S0022-1694(96)80030-8)
- Whitaker, S. (1986). Flow in porous media 1: A theoretical derivation of Darcy's law. *Transport in Porous Media*, 1, 3–25. <https://doi.org/10.1007/BF01036523>
- Yin, M. S., Zhang, Y., Ma, R., Tick, G. R., Bianchi, M., Zheng, C. M., et al. (2020). Super-diffusion affected by hydrofacies mean length and source geometry in alluvial settings. *Journal of Hydrology*, 582, 124515. <https://doi.org/10.1016/j.jhydrol.2019.124515>
- Zhang, Y., Baeumer, B., Chen, L., Reeves, D. M., & Sun, H. G. (2017). A fully subordinated linear flow model for hillslope subsurface storm-flow. *Water Resources Research*, 53, 3491–3504. <https://doi.org/10.1002/2016WR020192>
- Zhang, Y., Benson, D. A., & Baeumer, B. (2007). Predicting the tails of breakthrough curves in regional-scale alluvial systems. *Ground Water*, 45(4), 473–484. <https://doi.org/10.1111/j.1745-6584.2007.00320.x>

- Zhang, Y., Benson, D. A., & Reeves, D. M. (2009). Time and space nonlocalities underlying fractional derivative models: Distinction and literature review of applications. *Advances in Water Resources*, 32, 561–581. <https://doi.org/10.1016/j.advwatres.2009.01.008>
- Zhang, Y., Green, C. T., & Baeumer, B. (2014). Linking aquifer spatial properties and non-Fickian transport in alluvial settings. *Journal of Hydrology*, 512, 315–331. <https://doi.org/10.1016/j.jhydrol.2014.02.064>
- Zhang, Y., Zhou, D. B., Yin, M. S., Sun, H. G., Wei, W., Li, S. Y., & Zheng, C. M. (2020). Nonlocal transport models for capturing solute transport in one-dimensional sand columns: Model review, applicability, limitations and improvement. *Hydrological Processes*, 34, 5104–5122. <https://doi.org/10.1002/hyp.13930>
- Zhou, H. W., & Yang, S. (2018). Fractional derivative approach to No-Darcian flow in porous media. *Journal of Hydrology*, 566, 910–918. <https://doi.org/10.1016/j.jhydrol.2018.09.039>
- Zhou, H. W., Yang, S., & Zhang, S. Q. (2019). Modeling non-Darcian flow and solute transport in porous media with the Caputo–Fabrizio derivative. *Applied Mathematical Modelling*, 68, 603–615. <https://doi.org/10.1016/j.apm.2018.09.042>